

# Manifestation of spurious currents and interface regularization in wind turbulence over fast-propagating waves

Hanul Hwang and Catherine Górlé\*

*Center for Turbulence Research, Stanford University, California, USA 94305*

(Dated: February 23, 2026)

Accurate simulation of wind turbulence over fast-propagating waves requires interface-capturing methods that suppress numerical artifacts while accurately resolving momentum transfer across the interface. In high wave-age regimes, numerical errors at the air–water interface can reach magnitudes comparable to the physical flow, directly affecting predicted turbulence statistics. This study examines widely used interface-capturing techniques to evaluate how spurious currents and interface regularization influence wind–wave simulations through curvature estimation and flux discretization. A systematic assessment is performed using static and translating droplet benchmarks, together with solitary and monochromatic wave cases, to identify and quantify the dominant numerical error mechanisms. In addition, comparison with experimental measurements reveals how these primary error sources manifest in coupled wind–wave simulations. These findings clarify the numerical origin of the observed discrepancies and underscore the importance of accurate curvature and flux treatment in high wave-age regimes.

## I. INTRODUCTION

The study of wind–wave interaction has become increasingly important because of its central role in modern weather forecasting models and its influence on the resilience of coastal communities [1–3]. The complexity of this interaction arises from the dynamic evolution of the air–water interface, where mass, momentum, and energy are continuously exchanged. These exchanges occur across a wide range of spatial and temporal scales. At small scales, the interface undergoes distortion, breakup, and air entrainment, producing sea spray and ocean foam. At larger scales, the system encompasses long-fetch winds, gravity waves, and swells. The interplay between these scales creates a global coupling, in which small-scale interactions exert a significant influence on large-scale atmospheric and oceanic processes [4]. A detailed understanding of these multi-scale dynamics remains a major research priority, since accurate parameterization of small-scale momentum and scalar fluxes provides essential boundary conditions for numerical weather prediction models [5] and ocean forecasting systems [6, 7].

Computational approaches have played an important role in advancing this field by addressing limitations inherent to field measurements and laboratory experiments. Numerical simulations offer detailed and controllable environments for studying complex wind–wave interactions and have yielded insights not accessible through direct observation. These studies have validated existing theories and have also revealed new perspectives on the mechanisms that govern the transfer of momentum and energy across the air–sea interface. Direct numerical simulations (DNS) have, for example, ex-

amined wave-induced turbulent structures near the interface [8, 9]. The analysis of turbulent kinetic energy and Reynolds stress by Yang and Shen [9] demonstrated strong agreement with experimental observations. Large-eddy simulations have further expanded these capabilities. Sullivan *et al.* [10] introduced a broadband spectrum of time-varying finite-amplitude surface waves at the lower boundary to explore a wide range of wind conditions. The resulting wave-induced and turbulent wind stresses, and their contributions to total drag, have been examined in detail [11]. In addition, Cao and Shen [12] identified the vertical component of wave orbital velocity as the principal source of airflow and pressure perturbations, which play a pivotal role in shaping the spatial structure of the coupled system.

Despite these advances, most DNS and high-fidelity LES studies remain limited by their treatment of the air–water interface. Many investigations have focused exclusively on the wind flow while omitting explicit resolution of the interface [9, 12, 13]. Single-phase frameworks often approximate the interface through simplified boundary conditions [8], commonly imposing a lower boundary motion to mimic mild-sloped waves. In such formulations, the Navier–Stokes equations are solved in a wave-following coordinate system that restricts allowable wave slopes due to stability constraints associated with the Jacobian operator and that cannot represent surface drift. In other cases, wave effects are represented through localized form drag [14] or through empirical and potential-flow-based models derived from observations [15]. This simplification frequently excludes critical two-phase processes such as wave breaking, bubble entrainment, sea spray generation, and spume formation [16–18]. Neglecting these processes is particularly problematic in high-energy conditions, where the dynamics of breaking waves differ fundamentally from those of non-breaking waves [19–21]. High-fidelity simulations that explicitly address such small-scale dynamics remain limited, with only a few examples such as Yang *et al.*

---

\* Also at Civil and Environmental Engineering, Stanford University, California, USA 94305

[22]. Although two-phase simulations have been applied to more complex problems, including breaking waves and wave–structure interactions, many of these efforts are dominated by liquid-phase dynamics [23, 24] or rely on Reynolds-averaged Navier–Stokes models [25–27], which restrict their ability to represent detailed wind–wave coupling.

Realistic wind–wave simulations require accurate modeling of interface advection and surface-tension discretization. Such accuracy depends on reliable resolution of the air–water interface, which can be achieved through either explicit interface tracking or implicit interface-capturing. Several established approaches are available, including the level-set method [28], the volume-of-fluid (VOF) method [29], and the phase-field method [30, 31]. In this study, we focus on widely adopted interface-capturing methods implemented in multiphase-flow solvers such as OpenFOAM. The VOF framework in OpenFOAM includes geometric formulations, such as isoAdvector [32, 33], as well as algebraic formulations [34]. We investigate the manifestation of spurious currents arising from curvature-calculation errors and from interface-advection schemes used in flux evaluation, and assess their impact on wind–wave flow characteristics. By identifying the sensitivities associated with these numerical treatments, this study provides an essential step toward improving wind–wave interaction models and enhancing predictive capability for environmental and engineering applications.

This paper is organized as follows. Section II describes the governing equations and numerical models, including the interface-capturing techniques and post-processing procedures employed in this study. Section III presents canonical test cases, beginning with static drop simulations to evaluate curvature-calculation errors and assess grid-resolution effects, followed by moving-drop cases. Section IV investigates interface advection using solitary-wave simulations and practical monochromatic wave cases, with comparisons to experimental data. Conclusions are presented in Section V.

## II. GOVERNING EQUATIONS AND INTERFACE-CAPTURING METHODS

In this section, we describe the governing equations for fluid motion, followed by a comprehensive overview of interface-capturing methods used in this study. We then introduce the post-processing procedure for wind and wave simulation data using triple decomposition.

### A. Governing equations

The incompressible Navier-Stokes equations governing two immiscible fluids (phases1 and 2) are given by

$$\frac{\partial u_i}{\partial x_i} = 0, \quad (1)$$

$$\frac{\partial \rho u_i}{\partial t} + \frac{\partial \rho u_i u_j}{\partial x_j} = -\frac{\partial p^*}{\partial x_i} + \frac{\partial}{\partial x_j} \left( \mu_{\text{eff}} \frac{\partial u_i}{\partial x_j} \right) - g_j X_j \frac{\partial \rho}{\partial x_i} + \sigma \kappa \frac{\partial \phi}{\partial x_i}, \quad (2)$$

where  $\rho$  and  $u_i$  denote the density and velocity components, respectively. The pressure  $p^*$  is defined as  $p^* = p - \rho g_j X_j$ , where  $p$  represents the total pressure and  $g_j$  the gravitational acceleration. The term  $X_j$  corresponds to the position vector relative to a specified reference point. The effective viscosity,  $\mu_{\text{eff}}$ , is expressed as  $\mu_{\text{eff}} = \mu + \rho \nu_t$ , where  $\mu$  is the dynamic viscosity and  $\nu_t$  denotes the eddy viscosity. The phase indicator function,  $\phi$ , is used to distinguish between the two immiscible fluid phases. A value of  $\phi = 1$  denotes that the control volume is fully occupied by phase1, whereas  $\phi = 0$  corresponds to a region entirely filled with phase2. Based on this formulation, the local fluid properties are computed as

$$\rho = \rho_1 \phi + \rho_2 (1 - \phi), \quad (3)$$

$$\mu = \mu_1 \phi + \mu_2 (1 - \phi), \quad (4)$$

for density and viscosity, respectively.

The governing equations, Eqs. (1) and (2), are discretized using a finite-volume method on an unstructured mesh. Spatial discretization is carried out using a second-order central difference scheme, while temporal integration is performed using an implicit first order Euler method. The pressure-velocity coupling is achieved employing the pressure implicit with split operator (PISO) algorithm. The surface tension effect is included in the last term of Eq. (2), where  $\sigma$  denotes the surface tension coefficient,  $\kappa$  represents the interface curvature. We employ the continuum surface force (CSF) formulation proposed by Brackbill *et al.* [35], together with the balanced-force algorithm of Francois *et al.* [36].

### B. Interface modeling

The interface between two immiscible fluids is modeled using the VOF method, an interface-capturing method categorized under one-fluid models. We consider two variants of the VOF method: a geometric formulation based on isoAdvector [32, 33] and an algebraic formulation [37] employing the multidimensional universal limiter with explicit solution (MULES) [38]. Within the geometric formulation, two subclasses are examined, distinguished by their interface-reconstruction procedures. Although detailed algorithmic descriptions are available in the original references, the interface-capturing methods are outlined here to clarify differences in interface treatment. The reconstruction methods associated with the geometric formulation are further described in Appendix A.

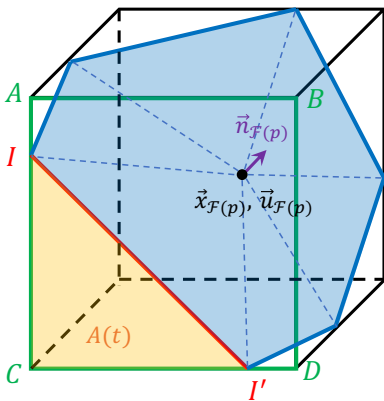


FIG. 1: A schematic of  $\phi_p$ -isoface.

### 1. Geometric VOF with isoAdvector

For the geometric VOF formulation isoAdvector, developed by Roenby *et al.* [32], the phase indicator  $\phi$  is transported according to

$$\frac{\partial \phi}{\partial t} + \frac{\partial u_i \phi}{\partial x_i} = 0. \quad (5)$$

Unlike the algebraic VOF transport equation below (e.g., see Eq.(12)), Eq.(5) does not include an artificial compression term.

In this approach, the face flux is computed based on geometric considerations of the interface, and the evolution of  $\phi$  is advanced in two steps. First, the interface is reconstructed within each computational cell. In a collocated framework, the phase indicator  $\phi$  is stored at the cell center. The reconstruction process seeks to determine a plane that divides the cell into two subregions, each occupied entirely by one phase. The objective is to ensure that the phase indicator, defined as the volume fraction of phase1 within a subcell, is consistent with the cell-centered volume fraction  $\phi_p$ , such that  $\phi_p = V_{\text{phase1}}/V_{\text{cv}}$ . As illustrated in Fig. 1, a cubic cell  $p$  (outlined in black) is intersected by iso-lines (blue lines), which constitute the periphery of the  $\phi_p$ -isoface. The geometric properties of the  $\phi_p$ -isoface, including its face center  $\mathbf{x}_{\mathcal{F}(p)}$ , face normal  $\mathbf{n}_{\mathcal{F}(p)}$ , and velocity vector  $\mathbf{u}_{\mathcal{F}(p)}$ , are then determined. Further details regarding the reconstruction schemes used in this study are provided in Section A.

In the second step, the face flux is computed based on the motion of the  $\phi_p$ -isoface. To update  $\phi$  from time step  $t_n$  to  $t_{n+1} = t_n + \Delta t$ , Eq. (5) is integrated over the control volume  $V_{\text{cv}}$  and in time as follows.

$$\phi^{n+1} = \phi^n - \frac{1}{V_{\text{cv}}} \sum_f \Delta V_f^n. \quad (6)$$

Here,  $\Delta V_f^n$  represents the volumetric face flux, which is approximated as

$$\Delta V_f^n \approx \frac{\Phi_f^n}{|S_{f,i}|} \int_{t_n}^{t_{n+1}} A(\tau) d\tau. \quad (7)$$

The face flux,  $\Phi_f$ , is given by  $\Phi_f = u_{f,i} S_{f,i}$ , where  $u_{f,i}$  and  $S_{f,i}$  represent the face-interpolated velocity and face normal vectors, respectively. In Eq. (7),  $A(\tau)$  represents the instantaneous area submerged by phase1.

As depicted in Fig. 1, if we calculate the volumetric face flux  $\Delta V_f$  in the green solid-line ABCD plane, the intersection between the ABCD plane and the  $\phi_p$ -isoface is marked as the red line  $\overline{II'}$ . The submerged area (highlighted in yellow) varies over time as the  $\phi_p$ -isoface propagates. The face-interface intersection  $\overline{II'}$  sweeps a quadrilateral (green square), leading to an expression for the submerged area  $A(\tau) = P_k \tau^2 + Q_k \tau + A_j(\tilde{t}_k)$ . Thus, the time integration of the submerged area  $A(\tau)$  in Eq. (7) is expressed as

$$\int_{t_n}^{t_{n+1}} A_j(\tau) d\tau = \sum_{k=1}^{N_v-1} \int_{\tilde{t}_k}^{\tilde{t}_{k+1}} A_j(\tau) d\tau, \quad (8)$$

where  $N_v$  denotes the total number of vertices in the corresponding cell. The time instances  $\tilde{t}_k$  represent the moments at which the  $\phi_p$ -isoface passes through each  $k^{\text{th}}$  vertex of the cell and are approximated as

$$\tilde{t}_k \approx t_n + (x_{k,i} - x_{\mathcal{F}(p),i}) \frac{n_{\mathcal{F}(p),i}}{u_{\mathcal{F}(p),i} n_{\mathcal{F}(p),i}}. \quad (9)$$

Here,  $x_{k,i}$  denotes the spatial coordinate of the  $k^{\text{th}}$  vertex, with  $k = 1, \dots, N_v$ . The quantities  $n_{\mathcal{F}(p),i}$  and  $u_{\mathcal{F}(p),i}$  refer to the components of the interface normal and the velocity of the  $\phi_p$ -isoface at its center. The definitions of these quantities are provided in Eq. (A2) for the interface normal and Eq. (A3) for the centroid in the following section. The velocity  $u_{\mathcal{F}(p),i}$  is obtained by linear interpolation of the velocities at the vertices of the tetrahedron that contains the point  $\tilde{\mathbf{x}}_{\mathcal{F}(p)}$ . The coefficients  $P_k$  and  $Q_k$  are polynomial terms computed from the geometric configuration of the  $\phi_p$ -isoface near each vertex. Additional details regarding their evaluation can be found in Roenby *et al.* [32]. Using this information, each integral term in Eq. (8) can be evaluated analytically as

$$\int_{\tilde{t}_k}^{\tilde{t}_{k+1}} A_j(\tau) d\tau = \frac{1}{3} (\tilde{t}_{k+1}^3 - \tilde{t}_k^3) P_k + \frac{1}{2} (\tilde{t}_{k+1}^2 - \tilde{t}_k^2) Q_k + (\tilde{t}_{k+1} - \tilde{t}_k) A_j(\tilde{t}_k). \quad (10)$$

The total flux associated with interface transport is necessary for the convection term in the momentum equation, Eq.(2). In isoAdvector approach, it is computed as

$$F_{\text{ISO}} = \frac{\Delta V_f}{\Delta t} (\rho_1 - \rho_2) + \Phi_f \rho_2. \quad (11)$$

The superscript  $n$  is dropped for simplicity. Since Eq.(6) integrates the volumetric flux in time, the first term in Eq.(11) is divided by  $\Delta t$ .

As a brief note on the isoAdvector method, it offers improved computational efficiency on unstructured

grids compared to conventional geometric VOF reconstruction approaches. Traditional methods, such as the Mixed Youngs-Centered scheme or the Efficient Least-Square Volume-of-Fluid Interface Reconstruction Algorithm, involve more complex interface reconstruction procedures [32]. In addition, isoAdvector bypasses the need for operator splitting or unsplit advection schemes, both of which can introduce significant parallel load imbalances in unstructured grid frameworks [39]. Despite these advantages, isoAdvector has been reported to generate larger spurious currents near the interface, an issue that is further analyzed below.

## 2. Algebraic VOF with MULES limiter

For the algebraic VOF approach, the transport equation for the phase indicator  $\phi$  is given by

$$\frac{\partial \phi}{\partial t} + \frac{\partial u_i \phi}{\partial x_i} + \frac{\partial \mathcal{U}_i \phi (1 - \phi)}{\partial x_i} = 0. \quad (12)$$

Here,  $\mathcal{U}_i$  represents the relative velocity between the two phases. The last term, commonly referred to as the compression term, is introduced to maintain a sharp interface representation. This term becomes active only in interface cells, where the phase indicator takes intermediate values,  $\phi \in (0, 1)$ , and operates in the direction normal to the interface.

To discretize the compression term, the normal component of  $\mathcal{U}_i$  is defined at the cell faces as

$$\mathcal{U}_{fn} = n_f C_\alpha \frac{|\Phi_f|}{|S_{f,i}|}. \quad (13)$$

The subscript  $f$  denotes values evaluated at cell faces. The coefficient  $C_\alpha$  controls the intensity of interface compression and is set to unity in the present study, unless stated otherwise. The term  $n_f$ , representing the dot product of the interface normal and the face normal vector  $S_{f,i}$ , is defined as

$$n_f = \left( \frac{\partial \phi}{\partial x_i} / \left| \frac{\partial \phi}{\partial x_i} \right| \right) S_{f,i}. \quad (14)$$

The discretized form of Eq. (12) within a finite-volume framework is written as

$$\frac{\phi^{n+1} - \phi^n}{\Delta t} V_{cv} + \sum_f \{ \phi_f^n F_L^n + \phi_f^n (1 - \phi_f^n) F_{NL}^n \} = 0. \quad (15)$$

Here,  $V_{cv}$  represents the control volume of a computational cell. The terms  $F_L$  and  $F_{NL}$  correspond to the flux contributions from the linear and nonlinear terms, respectively, and are defined as  $F_L = \Phi_f$  and  $F_{NL} = \mathcal{U}_{fn}$ . The face-interpolated phase indicator,  $\phi_f$ , is computed using a high-resolution scheme to maintain boundedness and accuracy of  $\phi$ . The superscripts  $n$  refers to the  $n^{\text{th}}$  time step. Equation (15) is solved iteratively using the

MULES solver [38] to preserve boundedness of the phase indicator, as accurate maintenance of a sharp interface is essential in two-phase flow simulations. This approach is based on Zalesak's limiter [40], where the weighting factors of the high-order (or antidiffusive) flux are determined iteratively.

The total flux associated with the transport of  $\phi$ , corresponding to the second term in Eq. (15), is calculated by solving

$$F_\phi^n = \phi_f^n F_L^n + \phi_f^n (1 - \phi_f^n) F_{NL}^n. \quad (16)$$

Further details on the MULES solver can be found in Márquez Damián *et al.* [38]. The values of  $\phi$  and  $F_\phi$  are updated at the end of each subcycle. Accordingly, the total flux for MULES, denoted by  $F_{\text{MULES}}$ , which accounts for both transport and compression of  $\phi$ , is computed as

$$F_{\text{MULES}} = \sum_{i=1}^{n_{sc}} \frac{\Delta t_{sc}}{\Delta t} F_{sc,i}, \quad (17)$$

where  $F_{sc,i}$  is given by

$$F_{sc,i} = F_\phi (\rho_1 - \rho_2) + F_L \rho_2. \quad (18)$$

The superscript  $n$  is dropped to be consistent with the expression Eq. (11). Finally, the computed total flux  $F_{\text{MULES}}$  is used to update the momentum equation.

## C. Phase-averaging and triple decomposition

To analyze the wind flow field over surface waves, a phase-averaging approach based on the Hilbert transform is employed to quantify the statistical properties of wind turbulence [41]. Assuming that the wave-coherent component and the turbulent fluctuations of the wind are sufficiently uncorrelated, the velocity field is decomposed into three distinct components: a phase-independent mean, a wave-coherent component, and a turbulent fluctuation component.

Consider a wave elevation field  $\eta(\mathbf{x}, t)$ . The corresponding analytic signal is defined as  $\eta(\mathbf{x}, t) + i\mathcal{H}\eta(\mathbf{x}, t)$ , where  $\mathcal{H}\eta(\mathbf{x}, t)$  denotes the inverse transform to physical space of the Hilbert transform of the wave signal evaluated in spectral space. The wave phase  $\Phi(\mathbf{x}, t)$  is then defined as

$$\Phi(\mathbf{x}, t) = \arg[\eta(\mathbf{x}, t) + i\mathcal{H}\eta(\mathbf{x}, t)]. \quad (19)$$

Once the unique phase of the wave signal is identified, the turbulent component  $\mathbf{u}'$  of the flow field  $\mathbf{u}$  is defined as

$$\mathbf{u}'(x, y, z, t) = \mathbf{u}(x, y, z, t) - \langle \mathbf{u} \rangle(\xi, \zeta), \quad (20)$$

where  $\langle \mathbf{u} \rangle(\xi, \zeta)$  denotes the phase-averaged velocity field in a wave-following coordinate system, and  $(x, y, z)$  and  $t$  represent the Cartesian coordinates and time, respectively. Fig. 2 illustrates the wave-following coordinate system along with the corresponding wave phase.

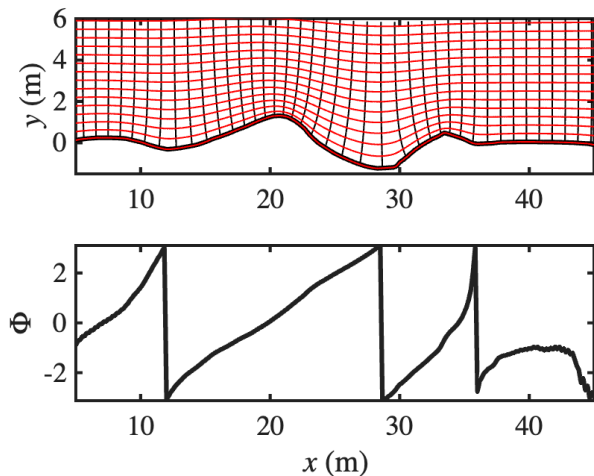


FIG. 2: (a) Illustration of the wave-following coordinate system  $(\xi, \zeta)$ , with  $\xi$  and  $\zeta$  represented by red and black solid lines, respectively. The wave surface is indicated by the thicker black solid line. (b) Corresponding wave phase  $\Phi$  (Eq. (19)) of the signal shown in (a).

The phase-averaged component is obtained as

$$\langle \mathbf{u} \rangle(\xi, \zeta) = \frac{1}{N_t N_z} \sum_{i=1}^{N_t} \sum_{j=1}^{N_z} \mathbf{u}(\xi - ct_i, y_j, \zeta, t_i), \quad (21)$$

where  $N_t$  and  $N_z$  are the number of temporal snapshots and the number of sampling planes in the spanwise direction, respectively.  $c$  is the wave celerity. It is assumed that the flow is statistically homogeneous in the spanwise direction. The total number of samples used in the averaging is  $N_{\text{samples}} = N_t \times N_z$ . The wave-following coordinate system and the procedure for computing the phase-averaged velocity field are described in detail in Section B.

The phase-averaged velocity field  $\langle \mathbf{u} \rangle(\xi, \zeta)$  is further decomposed into two components: a phase-independent mean  $\bar{\mathbf{u}}(\zeta)$  and a wave-coherent fluctuation  $\tilde{\mathbf{u}}(\xi, \zeta)$ . These are defined respectively as

$$\bar{\mathbf{u}}(\zeta) = \frac{1}{N_\xi} \sum_{k=1}^{N_\xi} \langle \mathbf{u} \rangle(\xi_k, \zeta), \quad (22)$$

and

$$\tilde{\mathbf{u}}(\xi, \zeta) = \langle \mathbf{u} \rangle(\xi, \zeta) - \bar{\mathbf{u}}(\zeta), \quad (23)$$

where  $N_\xi$  is the total number of discretized points in the  $\xi$  direction.

As a result, the instantaneous velocity field in the air domain can be expressed using the triple decomposition as

$$\mathbf{u}(x, y, z, t) = \bar{\mathbf{u}}(\zeta) + \tilde{\mathbf{u}}(\xi, \zeta) + \mathbf{u}'(x, y, z, t), \quad (24)$$

as summarized in Fig. 3. The first term represents the phase-independent mean flow, the second term accounts

for the wave-coherent modulation, and the third term corresponds to the turbulent fluctuations.

It is important to note that the triple decomposition is applicable only to statistically stationary flows. Furthermore, accurate statistical convergence of the phase-averaged and wave-coherent components requires a sufficiently large number of samples within each phase bin. In this study, we employed  $N_{\text{bins}} = 100$  and ensured a total sample size of  $N_{\text{samples}} > 1000$ .

### III. CANONICAL TEST CASES AND RESULTS

In the discussion of results, the following abbreviations are adopted for the three interface-capturing methods used throughout the subsequent sections. The geometric VOF-type method with  $\phi$ -based interface reconstruction is referred to as the `isoPhi` method. The reconstructed distance function (RDF)-based geometric VOF method is denoted as `plicRDF`. The algebraic VOF-type method using the MULES limiter is referred to as `gradPhi`.

#### A. Static drop

We conduct classical static circular interface simulations to assess the accuracy of interface representation across different interface-capturing methods. In the presence of an interface, inaccuracies in its representation can lead to numerical errors in the velocity field near the interface, commonly referred to as spurious currents. These spurious currents originate from an imbalance between the surface tension force and the pressure gradient across the interface [35]. When the surface tension and pressure gradient terms are consistently discretized [36], they should ideally cancel each other out, provided the interface curvature is computed exactly. This canonical test case is thus employed to verify the correctness of the code implementation and to quantify curvature-related errors through the manifestation of spurious currents across different interface-capturing methods. In what follows, we refer to the static circular interface simply as a drop for brevity.

##### 1. Simulation setup

The drop test case configuration follows that of Abadie *et al.* [42]. A two-dimensional domain of size  $[-1, 1] \times [-1, 1]$  m is considered, containing a stationary circular drop of diameter  $D_{\text{drop}} = 0.8$  m centered at  $(x, y) = (0, 0)$  m. The surface tension coefficient is set to unity. Both viscosity and density ratios are set to one, with  $\rho_{\text{drop}} = 1$  kg/m<sup>3</sup> and  $\mu_{\text{drop}} = 8.165 \times 10^{-3}$  Pa · s, corresponding to a Laplace number of  $La = \rho_{\text{drop}} D_{\text{drop}} \sigma / \mu_{\text{drop}}^2 = 12000$ . The domain is discretized using  $N = 64$  grid points in each direction, and a time

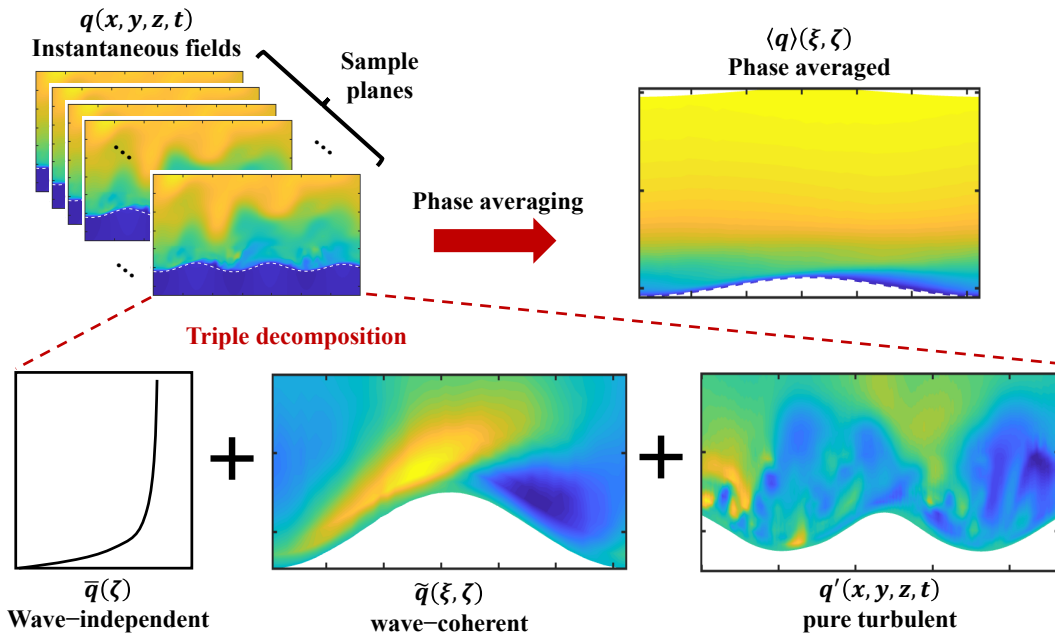


FIG. 3: Schematic of the triple decomposition. The phase-averaged field  $\langle \mathbf{u} \rangle(\xi, \zeta)$  is obtained from  $N_{\text{samples}}$  snapshots, and the velocity field is decomposed into the wave-independent component  $\bar{\mathbf{u}}(\zeta)$  (Eq. (22)), the wave-coherent component  $\tilde{\mathbf{u}}(\xi, \zeta)$  (Eq. (23)), and the turbulent component  $\mathbf{u}'(x, y, z, t)$  (Eq. (20))

step of  $\Delta t = 0.00065$  s is used. Symmetry boundary conditions are imposed on the lateral boundaries, and periodic boundary conditions are applied on the top and bottom boundaries. Simulations are performed up to  $t = 102.86 t_\sigma$ , where  $t_\sigma = \sqrt{\rho_{\text{drop}} D_{\text{drop}}^3 / \sigma}$  is the characteristic capillary time, corresponding to  $t = 72$  s.

## 2. Spurious current

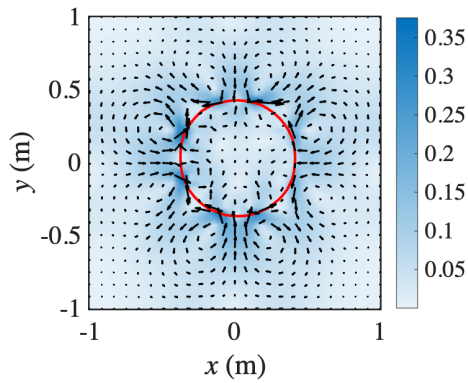
Fig. 4 shows the velocity fields at  $t = 10.21 t_\sigma$ , visualized using colormaps for magnitude and vectors for direction. Note that the colorbar scale differs between subfigures to reflect the range of spurious current magnitudes. The maximum spurious velocity in the **isoPhi** method is on the order of  $O(10^{-1})$  (Fig. 4(a)). In comparison, the **plicRDF** and **gradPhi** methods yield significantly lower maximum spurious velocities, on the order of  $O(10^{-4})$  and  $O(10^{-3})$ , respectively. The **plicRDF** method achieves three orders of magnitude lower spurious velocity than the **isoPhi** method due to its more accurate curvature estimation by the RDF. The lower spurious current in the **gradPhi** method is attributed to the smearing of the interface, controlled by the compression velocity  $U_i$  in Eq. (12), which facilitates more stable curvature calculations.

For a more quantitative assessment, Fig. 5 presents curvature and pressure profiles along the horizontal centerline ( $y = 0$ ) and the diagonal line ( $y = x$ ). The interface location is marked with vertical gray lines, and the

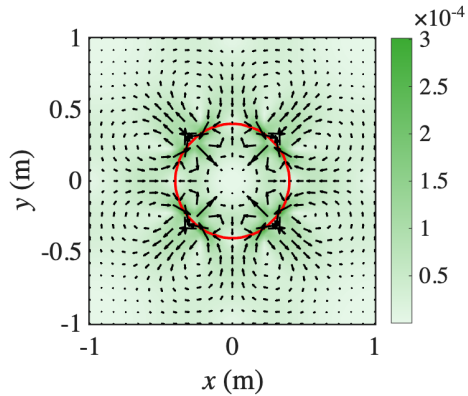
initial phase indicator  $\phi$  is shown in yellow circles. The exact curvature is  $\kappa = 2/D_{\text{drop}} = 2.5 \text{ m}^{-1}$ , and the corresponding pressure jump is given by the Young–Laplace law as  $\Delta p = \sigma \kappa = 2.5 \text{ Pa}$ . Reference values for  $\phi$ ,  $\kappa$ , and  $\Delta p$  are indicated by horizontal gray-dashed lines.

The pressure jump for the **isoPhi** method is approximately  $\Delta p \approx 2.1 \text{ Pa}$ , with curvature  $\kappa \simeq 2 \text{ m}^{-1}$  along  $y = 0$ , but significant deviation is observed along  $y = x$ . Moreover, the symmetry of the solution breaks down, as the large spurious currents distort the drop shape. The most accurate results are obtained using the **plicRDF** method, which yields an exact pressure jump of  $\Delta p = 2.5 \text{ Pa}$  and excellent agreement in curvature along both  $y = 0$  and  $y = x$ , as shown in Fig. 4(b). The **gradPhi** method preserves symmetry across both directions, with a slightly improved pressure jump of  $\Delta p \approx 2.2 \text{ Pa}$ . The curvature is accurately predicted along  $y = 0$ , though it deviates by approximately 20% along  $y = x$ .

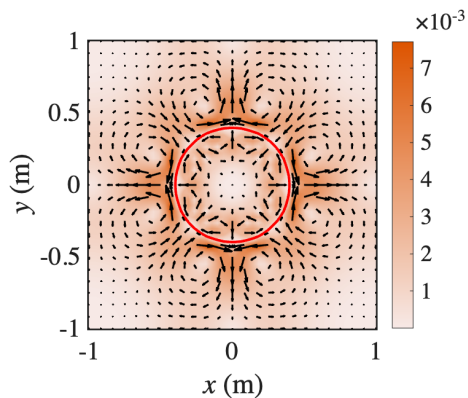
The long-term effects of spurious currents can be significant in wind–wave configurations, as they continuously influence the wind field within a confined region. To further evaluate the spurious current behavior in a long time duration, the nondimensional capillary number is defined as  $Ca_{\text{max}} = \mu_{\text{drop}} U_{\text{max}} / \sigma$ , where  $U_{\text{max}}$  is the maximum velocity magnitude in the domain. Fig. 6 shows the evolution of  $Ca_{\text{max}}$  for each method. The observed magnitudes are consistent with those reported in Gamet *et al.* [43] for a Laplace number of  $La = 12000$ . It is also noted that the initial time steps of both **isoPhi** and **gradPhi** exhibit identical capillary numbers. Although not shown here, we note that the magnitude of the spurious current



(a)



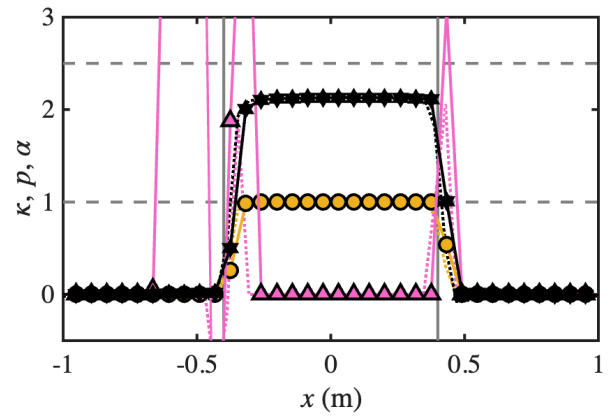
(b)



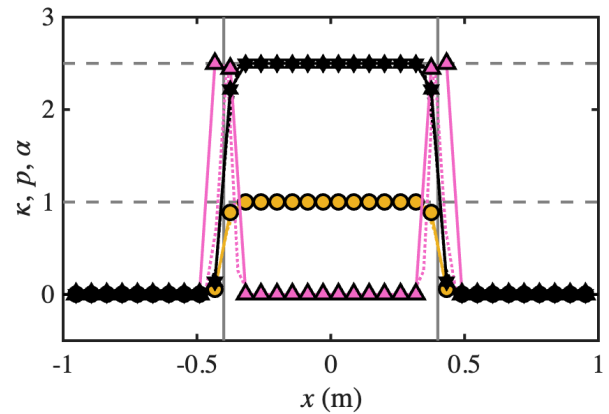
(c)

FIG. 4: Snapshots of static drop simulations using (a) `isoPhi`, (b) `plicRDF`, and (c) `gradPhi` at  $t = 10.21t_\sigma$ . Colormaps indicate the velocity magnitude, and black arrows represent the velocity vector field. The drop interface, defined by the  $\phi = 0.5$  contour, is shown with red solid lines.

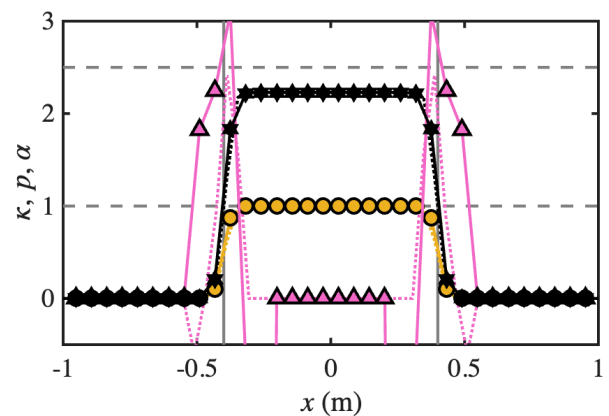
scales proportionally with the Laplace number. Specifically, the spurious current increases with higher drop density and surface tension, and decreases with higher drop viscosity. This trend is consistent with results from additional static drop simulations performed using non-unity viscosity and density ratios.



(a)



(b)



(c)

FIG. 5: Curvature (pink triangle lines) and pressure jump (black hexagram lines) extracted at  $t = 10.21t_\sigma$  along the horizontal line  $y = 0$  m (dotted lines) and the diagonal line  $y = x$  (solid lines) for (a) `isoPhi`, (b) `plicRDF`, and (c) `gradPhi`. The phase indicator  $\phi$  is shown in yellow circles. Vertical gray solid lines denote the expected interface location ( $\phi = 0.5$ ), and horizontal gray-dashed lines indicate reference values for curvature and pressure jump.

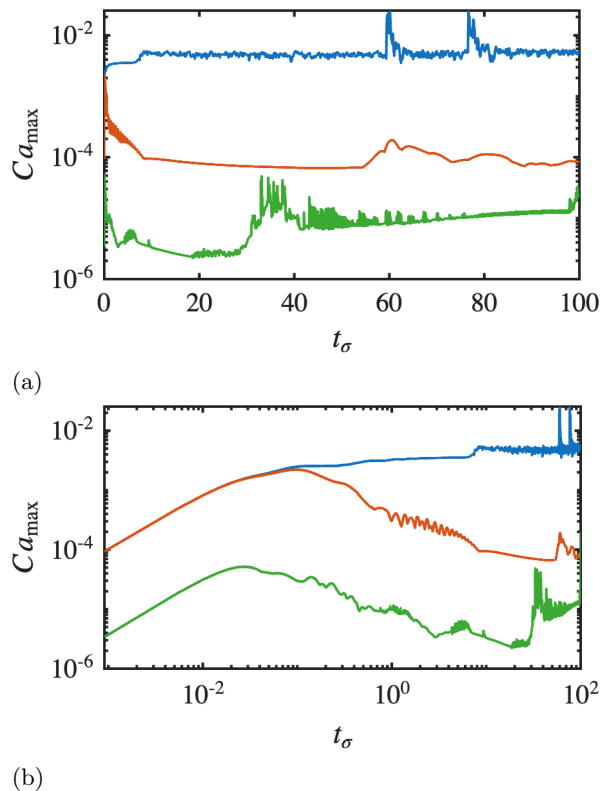


FIG. 6: Time evolution of the maximum capillary number  $Ca_{\max}$  for the static drop simulations shown in (a) linear and (b) logarithmic scale. Results are shown for **isoPhi** (blue), **plicRDF** (green), and **gradPhi** (red) methods.

### 3. Curvature error scaling

As an extension of the classical static drop analysis, we define errors associated with curvature, interface normal, and pressure jump calculations, and investigate how these errors scale with grid resolution.

This analysis is particularly important for wind-wave simulations, where the common approach to resolving small-scale wind turbulence near the interface is to refine the grid locally. In this context, it is desirable for the spurious current magnitude to decrease, or at least not increase, as the grid is refined. However, increased resolution can amplify curvature errors and associated spurious currents, especially in models lacking curvature converging techniques [44]. This issue becomes even more critical in unstructured grid frameworks, where accurate curvature estimation is not only more difficult but also computationally expensive.

Given the simple circular geometry of the drop, exact analytical values of curvature, interface normal, and pressure jump are known. The curvature error is defined using both infinity-norm and 1-norm-like metrics as follows:

$$\mathcal{E}_\kappa^\infty = \max_i \frac{|\kappa_i - \kappa_{\text{exact}}|}{\kappa_{\text{exact}}}, \quad \mathcal{E}_\kappa^1 = \frac{1}{N_i} \sum_i \frac{|\kappa_i - \kappa_{\text{exact}}|}{\kappa_{\text{exact}}}, \quad (25)$$

where  $i$  denotes the index of interfacial cells and  $N_i$  is the total number of such cells. Similarly, the pressure error is defined as:

$$\mathcal{E}_p^\infty = \max_i \frac{|p_i - p_{\text{exact}}|}{p_{\text{exact}}}, \quad \mathcal{E}_p^1 = \frac{1}{N_i} \sum_i \frac{|p_i - p_{\text{exact}}|}{p_{\text{exact}}}. \quad (26)$$

The interface normal error is quantified by:

$$\mathcal{E}_n^\infty = \max_i (1 - n_i \cdot n_{\text{exact},i}),$$

$$\mathcal{E}_n^1 = \frac{1}{N_i} \sum_i (1 - n_i \cdot n_{\text{exact},i}). \quad (27)$$

Fig. 7 presents these errors, along with the maximum spurious current magnitude  $|u|_{\max}$  and its spatial average  $\overline{|u|_{\max}}$ , across various grid resolutions. All other simulation parameters are kept constant while the number of grid points  $N$  is varied logarithmically across ten cases:  $N = 125, 162, 208, 269, 348, 449,$  and  $580$ . Data is collected at 100-th time steps, allowing interface-capturing methods to converge sufficiently before the onset of large spurious motion.

Fig. 7(a) shows that the curvature errors for the **isoPhi** and **gradPhi** methods increase linearly with grid refinement, following a  $\Delta x^{-1}$  scaling (black dashed line). In contrast, the **plicRDF** method exhibits much smaller errors, two orders of magnitude lower, and remains largely insensitive to grid resolution. Interface normal errors, shown in Fig. 7(b), converge with a rate close to  $\Delta x^2$  across all methods. However, the **isoPhi** method displays one order of magnitude higher error than the **gradPhi** and **plicRDF** methods. For pressure jump errors, the **gradPhi** method slightly outperforms **isoPhi**, while the **plicRDF** method again shows the most accurate results, with two orders of magnitude lower error. These trends are mirrored in the spurious current magnitudes, which increase with grid resolution for all methods, though not as steeply as the curvature errors. The most noticeable increase is observed in the **isoPhi** method. Across all resolutions, the **isoPhi** method exhibits the highest errors, while the **plicRDF** method consistently yields the most accurate results.

## B. Moving drop

The previous test cases considered static interfaces with unity viscosity and density ratios. In this section, we investigate large density and viscosity ratio settings along with non-zero surface tension. The interface is advected over a short time interval to evaluate the importance of the induced velocity manifested differently across interface-capturing methods, with emphasis placed on relative differences rather than on the absolute magnitude of spurious currents.

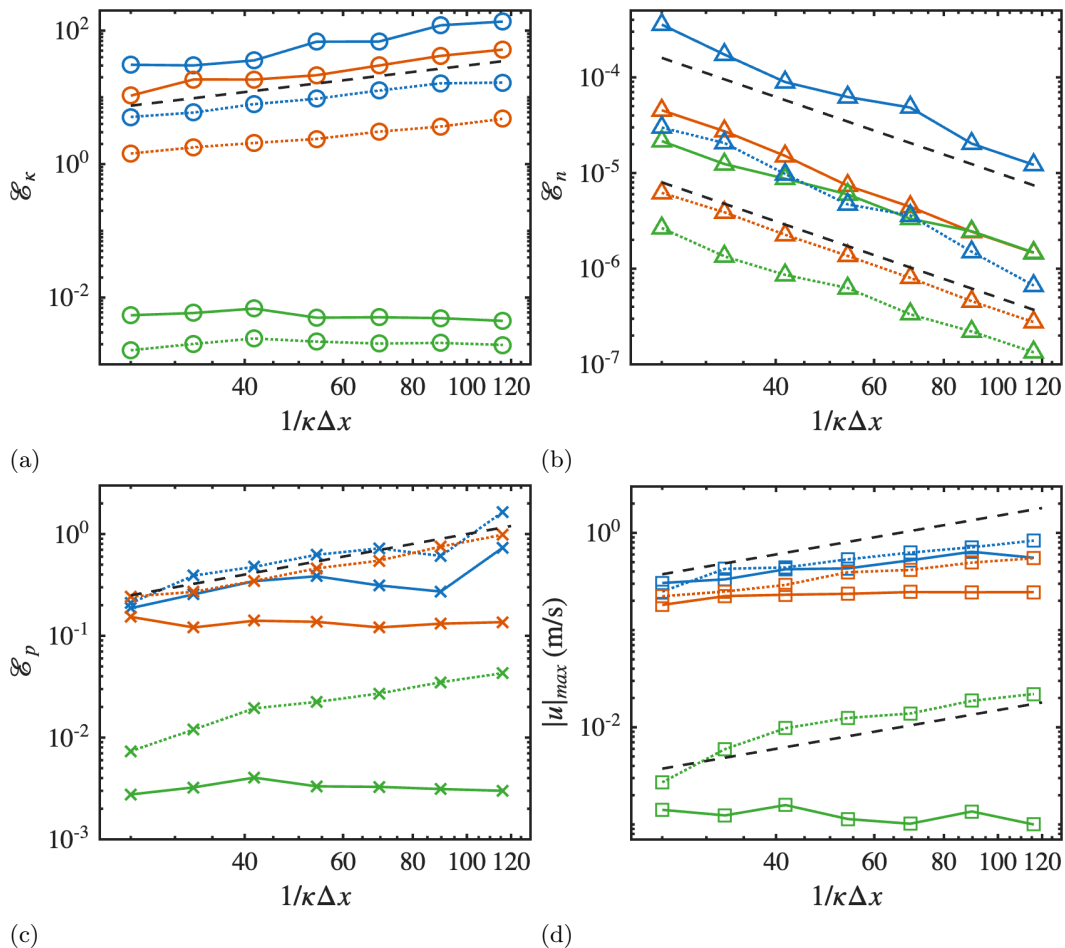


FIG. 7: Error metrics for (a) curvature, (b) interface normals, (c) pressure jump, and (d) maximum magnitude of spurious current as functions of grid resolution for **isoPhi** (blue), **plicRDF** (green), and **gradPhi** (red). Solid lines indicate infinity-norm-like errors, while dotted lines represent 1-norm-like errors. Reference scaling trends are shown with black dashed lines:  $\Delta x^{-1}$  in panels (a), (c), and (d), and  $\Delta x^2$  in panel (b).

### 1. Simulation setup

The numerical setup for the moving drop cases is identical to that of the static drop cases in Section III A, except for four modifications. First, the density of the fluid inside the circular drop is set to  $\rho_{\text{circle}} = 998 \text{ kg/m}^3$ , and that of the surrounding fluid is  $\rho_{\text{sur}} = 1.2 \text{ kg/m}^3$ , representing water and air, respectively. Second, the surface tension is set to  $\sigma = 0.072 \text{ N/m}$ . Third, the initial velocity of the drop is assigned a finite uniform value in the  $-\hat{y}$  direction. Lastly, the time step is fixed at  $\Delta t = 0.005 \text{ s}$ . Simulations are run for 10 time steps, corresponding to a physical time of  $t = 0.05 \text{ s}$ . This brief duration ensures the drop maintains an approximately circular shape while minimizing the influence of the interface advection term. The drop shifts slightly downward, and its new center is identified. We verified that the drop’s geometry remains nearly circular at this time.

The **isoPhi** results are set as a reference and define

the velocity difference metric relative to it as

$$\mathcal{D}_{\text{md}} = \frac{\left\{ \frac{1}{N_{\text{cv}}} \sum_i (u_i - u_{\text{isoPhi},i})^2 \right\}^{1/2}}{u_{\text{center}}}, \quad (28)$$

where  $N_{\text{cv}}$  is the number of control volumes and  $u_{\text{center}}$  is the bulk velocity of the drop. We emphasize that Eq. (28) does not represent an error, but rather a metric quantifying the difference between **plicRDF** and **gradPhi** relative to **isoPhi**. Because **plicRDF** provides enhanced curvature-calculation accuracy, whereas **gradPhi** employs a different numerical flux formulation, comparisons with **isoPhi** isolate how these factors manifest in the present setting.

### 2. Velocity field comparison

Fig. 8 presents the velocity field differences for the **plicRDF** and **gradPhi** methods relative to **isoPhi**, with

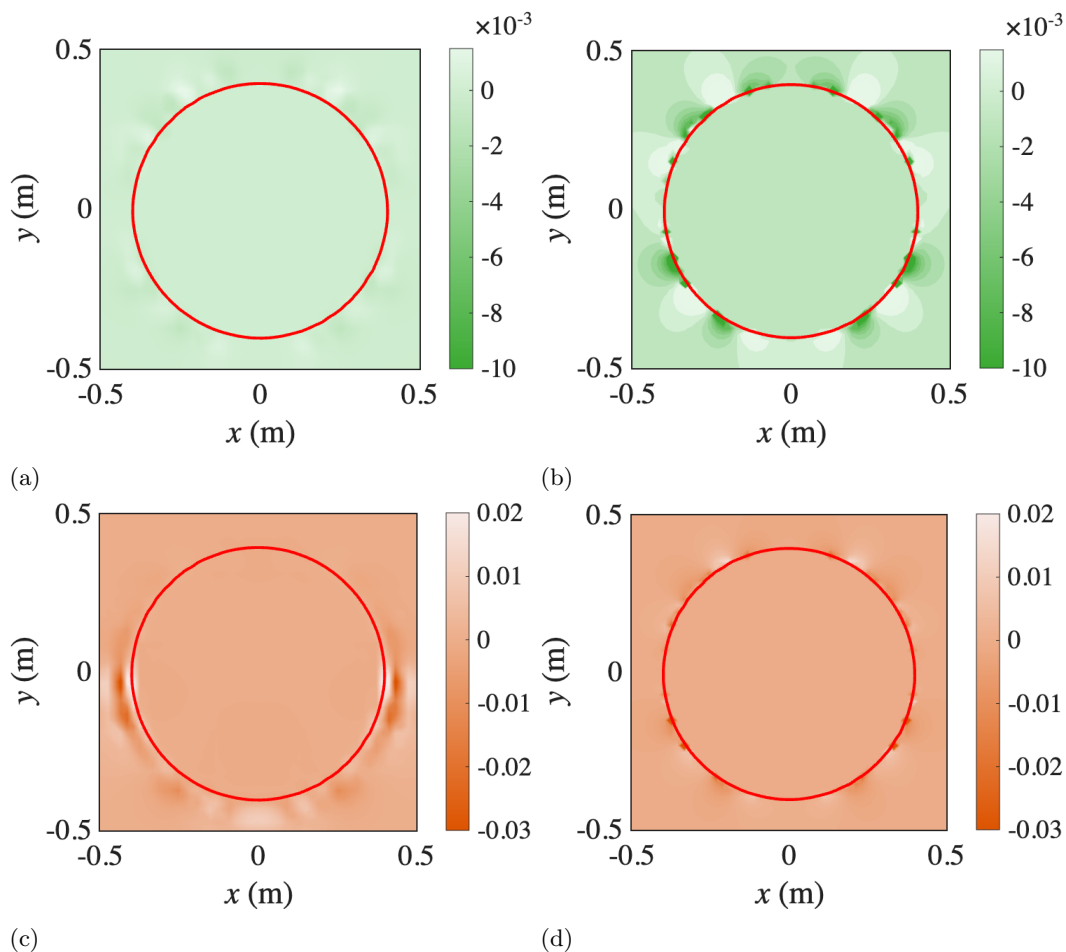


FIG. 8: Velocity difference fields for **plicRDF** (first row) and **gradPhi** (second row) after 100 time steps, relative to the **isoPhi** approach. The first and second columns correspond to grid resolutions of  $N_x = 64$  and  $N_x = 1024$ , respectively. The interface, defined by the  $\phi = 0.5$  contour, is indicated by the red solid line.

the first and second rows corresponding to each method, respectively. The first and second columns correspond to coarse ( $N_x = 64$ ) and fine ( $N_x = 1024$ ) grid resolutions. Additionally, Fig. 9 shows the velocity magnitude along a ring at  $r = 1.01R_{\text{drop}}$ , where  $R_{\text{drop}}$  is the initial drop radius, as a function of the polar angle  $\theta$ , measured counterclockwise from  $\vec{n} = (1, 0)$ .

For the coarse grid, **plicRDF** (Fig. 8(a)) shows negligible velocity difference, with a maximum difference  $\mathcal{D}_{\text{md}} \sim O(10^{-3})$ . In contrast, the **gradPhi** method (Fig. 8(c)) exhibits pronounced velocity differences near  $\theta = 0$  and  $\pi$ , as well as in the region  $\theta \in [\pi, 2\pi]$ , with magnitudes an order of magnitude larger. This difference persists regardless of grid resolution and is addressed in the following section. These trends are confirmed in Fig. 9(a), where **gradPhi** displays larger velocity magnitudes at  $\theta = 0$  and  $\pi$ , while all other methods show consistent velocity distributions.

With grid refinement, the difference between **isoPhi** and **plicRDF** increases significantly, as shown in Fig. 8(b). This increase in  $\mathcal{D}_{\text{md}}$  is attributed to amplified

spurious currents in the **isoPhi** method, consistent with curvature error trends discussed in Section III A 3. This is further supported by Fig. 9(b), where **isoPhi** shows higher velocity fluctuations across all angles. In contrast, the velocity difference for the **gradPhi** method at  $\theta = 0$  and  $\pi$  decreases with grid refinement, gradually converging toward the velocity profile of the **plicRDF** method.

Given the sensitivity of  $\mathcal{D}_{\text{md}}$  to resolution, we further evaluate its behavior for grid resolutions  $N_x = 64, 128, 256, 512,$  and  $1024$  in Fig. 10(a). For **plicRDF**, the velocity difference increases with grid refinement, whereas coarse grids yield nearly identical velocity fields ( $\mathcal{D}_{\text{md}} \simeq 10^{-3}$ ). This behavior, combined with earlier findings, highlights the strong link between curvature error and velocity fluctuations near the interface. For the **gradPhi** method, the trend is non-monotonic.  $\mathcal{D}_{\text{md}}$  decreases initially, then increases again with further refinement. At coarse resolution, the dominant velocity error stems from compression-induced artifacts near  $\theta = 0$  and  $\pi$ . At finer resolution, the primary contribution to  $\mathcal{D}_{\text{md}}$  shifts toward increased spurious currents in the **isoPhi**

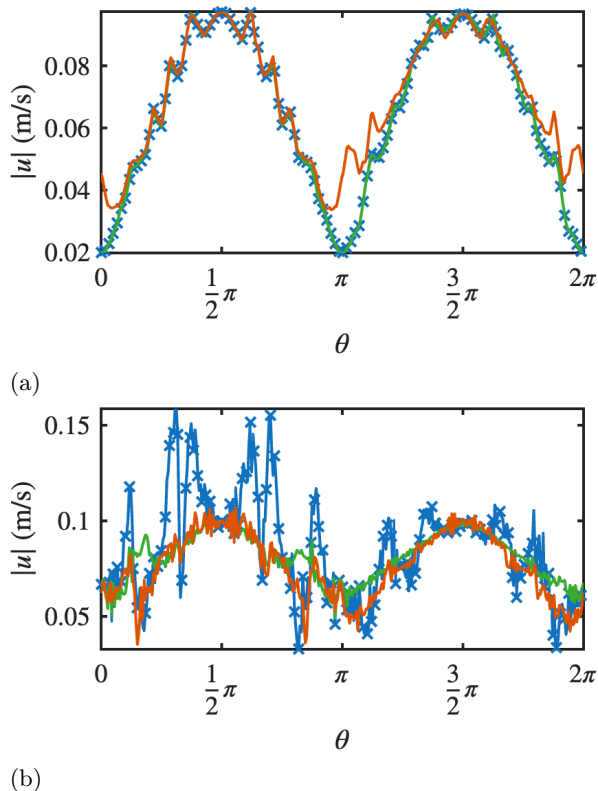


FIG. 9: Velocity magnitude measured along a circular path located at  $r = 1.01R_{\text{drop}}$  from the drop center after 100 time steps. The angular position is measured counterclockwise from the vector  $\mathbf{n} = (1, 0)$ . The `isoPhi` result is shown as a blue solid line with cross symbols, while `plicRDF` and `gradPhi` results are shown in green and red solid lines, respectively.

reference solution.

To further examine the importance of drop speed, we vary the initial speed of the drop while fixing the grid resolution at  $N_x = 512$  and  $N_y = 256$ . The drop speed is changed to  $|u|_{\text{center}} = 0.1, 0.3, 0.6,$  and  $1.0$  m/s. The resulting velocity difference  $\mathcal{D}_{\text{md}}$  are shown in Fig. 10(b). For the `plicRDF` method, as the drop velocity increases, the relative importance of velocity fluctuation errors decreases significantly. This indicates that numerical errors from inaccurate curvature estimation become significant only when the spurious current is on the same order of magnitude as the bulk velocity. In other words, when the interface moves sufficiently fast compared to the magnitude of the spurious current, its impact becomes negligible. For the `gradPhi` method, however,  $\mathcal{D}_{\text{md}}$  remains nearly constant regardless of drop velocity. Since the grid is fixed, this invariance implies that  $\mathcal{D}_{\text{md}}$  is not caused by spurious currents, but rather by excessive velocities introduced by the compression term. This issue will be addressed in more detail in the following section.

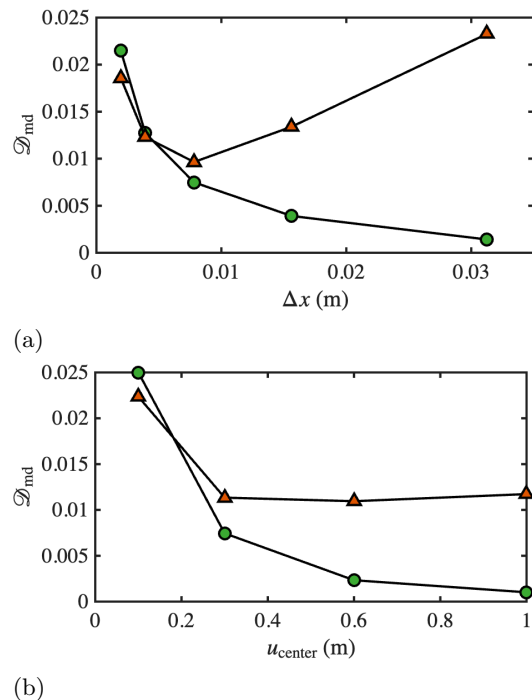


FIG. 10: Velocity difference metric  $\mathcal{D}_{\text{md}}$  for `plicRDF` (green circles) and `gradPhi` (red triangles) as a function of (a) grid resolution and (b) drop velocity  $|u_{\text{center}}|$ .

#### IV. WAVE TEST CASES AND RESULTS

We next examine the influence of interface advection on the flow field through the numerical discretization of the flux term. The `isoPhi` and `plicRDF` schemes employ the flux formulation given in Eq. (11), whereas the `gradPhi` method with MULES adopts the formulation in Eq. (17).

##### A. Sensitivity on interface advection: solitary wave

A solitary wave is a single, isolated wave propagating under conditions relevant to wind–wave interaction. It exhibits relatively high propagation speed over a large spatial scale, with negligible surface-tension effects. To isolate advection effects, we simulate a two-dimensional solitary wave in a periodic domain over a short duration, thereby minimizing the influence of inherently three-dimensional effects.

###### 1. Simulation setup

We consider a rectangular domain of dimensions  $L_x = 72.6$  m (horizontal) and  $L_y = 2.2$  m (vertical), discretized with uniform grid resolution of  $N_x = 2112$  and  $N_y = 110$  in the horizontal and vertical directions, respectively. Boundary conditions are prescribed as follows. For vali-

dation purposes, an Neumann boundary condition is applied at the top in the inviscid case. In addition, a viscous case with a slip boundary condition at the top is considered to investigate the kinetic energy of each phase, as discussed below. Periodic conditions are imposed on the lateral boundaries, and a no-slip condition is enforced at the bottom wall.

The velocity and interface fields are initialized using the second-order approximation to solitary wave theory by Laitone [45]. The initial wave elevation is given by

$$\eta = \frac{A}{H} S^2 - \frac{3}{4} \left( \frac{A}{H} \right)^2 S^2 (1 - S^2), \quad (29)$$

and the horizontal and vertical velocity components are

$$\begin{aligned} \frac{u}{\sqrt{gH}} &= \frac{A}{H} \left\{ 1 - \frac{5}{4} \frac{A}{H} - \frac{3}{2} \frac{A}{H} (2y + y^2) \right\} S^2 \\ &+ \left( \frac{A}{H} \right)^2 \left\{ \frac{5}{4} + \frac{9}{4} (2y + y^2) \right\} S^4, \quad (30) \\ \frac{v}{\sqrt{gH}} &= \sqrt{3 \left( \frac{A}{H} \right)^3} (1 + y) S^2 T \left\{ 1 - \frac{7}{8} \right. \\ &\left. \frac{A}{H} - \frac{1}{2} \frac{A}{H} (2y + y^2) - \frac{1}{2} \frac{A}{H} (1 - 6y - 3y^2) S^2 \right\}, \quad (31) \end{aligned}$$

where  $S^2 = \text{sech}^2(\tilde{x})$ ,  $S^4 = \text{sech}^4(\tilde{x})$ , and  $T = \tanh(\tilde{x})$ . The wave coordinate defined as

$$\tilde{x} = (x - x_0) \sqrt{\frac{3A}{4H}} \left( 1 - \frac{5A}{8H} \right). \quad (32)$$

Here,  $A$  and  $H$  denote the wave amplitude and mean water depth, respectively, and  $x_0 = 15$  m sets the initial wave peak location. Gravity is denoted by  $g = 9.8$  m/s<sup>2</sup>. A snapshot of the initial configuration is shown in Fig. 11(a). Simulations are carried up to  $t = 20$  s.

## 2. Interface regularization effects

Interface elevations are recorded at five probe locations ( $x = 30, 40, 50, 60,$  and  $70$  m) and shown in Fig. 11(b). In this inviscid case with zero surface tension, the solitary wave is expected to maintain its shape and kinetic energy as it propagates. Results from all three interface-capturing methods (symbols) closely match the theoretical solution (solid lines), indicating that interface transport is largely unaffected by the choice of method under these idealized conditions. This conclusion also extends to cases where inertial effects dominate over viscous and capillary forces. For example, we confirmed that under realistic density ratios ( $\rho_{\text{water}}/\rho_{\text{air}} \sim O(10^3)$ ) and small but non-zero surface tension ( $\sigma = 0.072$  N/m), interface advection accuracy remains robust across all schemes, with errors below 0.2%.

However, the effect of the choice of numerical scheme on the low-density (air) phase is more pronounced. To

assess this sensitivity, we compare the face fluxes from the `isoPhi` and `gradPhi` methods (Eqs. (11) and (17)). Due to the coarse grid resolution, `isoPhi` and `plcrDF` yield nearly identical results (see Section III B), so we focus on differences only with `isoPhi`.

Fig. 12 shows the flux difference  $F_{\text{MULES}} - F_{\text{ISO}}$  near the crest of the solitary wave. For  $A = 0.3$  m and  $H = 1$  m (Fig. 12(a)), a positive flux difference layer is observed above the crest with thickness comparable to the interface. A similar pattern appears for a smaller wave ( $A = 0.1$  m, Fig. 12(b)). The associated crest velocities are  $u_{\text{crest}} = 0.337$  and  $0.1$  m/s for  $A/H = 0.3$  and  $0.1$ , respectively. These results suggest that the extra momentum flux introduced in `gradPhi` is aligned with the wave direction and scales with the advection speed of the interface. This excess flux originates from the interface compression term, which artificially increases momentum transfer in mixed cells ( $0 < \phi < 1$ ). The magnitude of this effect is governed by the compression velocity in Eq.(13).

To confirm this behavior, we conduct additional simulations for  $A/H = 0.3$  with varying compression coefficients:  $C_\alpha = 0.1, 1.0,$  and  $2.0$ . Lower  $C_\alpha$  results in a thicker interface and a more pronounced excess flux layer, while higher  $C_\alpha$  yields a thinner interface and reduced flux anomaly. This phenomenon is further supported by the kinetic energy distribution across the two phases, as shown in Fig. 13. The total kinetic energy of each phase, calculated as  $K_{1,2} = \alpha_{1,2} \sum \frac{1}{2} \rho u_i^2, dV$ , indicates that lower  $C_\alpha$  results in higher kinetic energy in the air phase and more rapid decay in the water phase, reflecting artificial momentum transfer across the interface.

This artificial momentum transfer aligns with observations from Section III B, where `gradPhi` shows elevated velocity at  $\theta = 0$  and  $\pi$  (Fig. 8(c)), locations where the interface normal is orthogonal to the advection direction, similar to wave crests. When the grid is under-resolved, such flux artifacts significantly affect fast-moving interfaces.

## B. Monochromatic waves with high wave age

In this section, we examine a more practical configuration involving simulations of monochromatic waves with high wave age. Using the triple-decomposition framework described in Section II C, we analyze phase-averaged fields and stress distributions for all three interface-capturing methods. Two monochromatic wave scales are considered: a reference scale and a larger scale. This comparison is used to demonstrate how the observations discussed in Section IV A manifest across different geometric scalings.

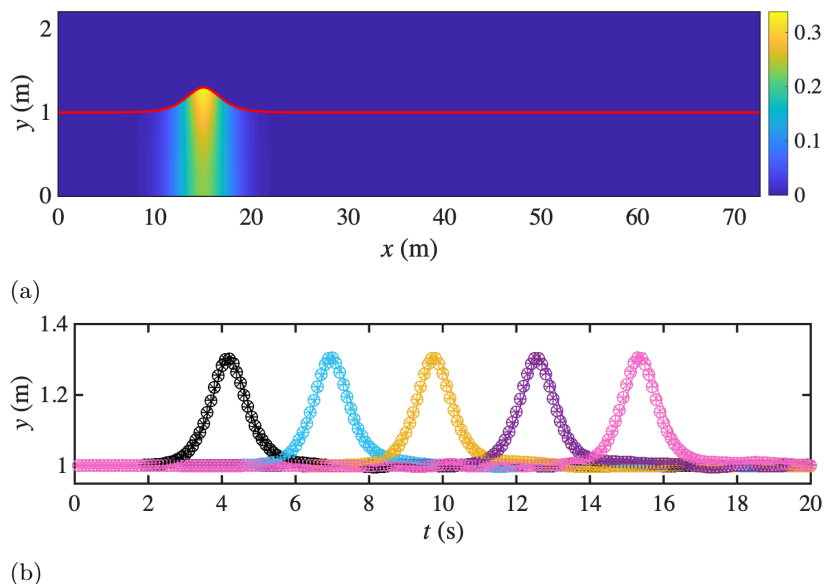


FIG. 11: (a) Initial condition for the solitary wave simulation. The velocity magnitude is shown as a colormap, and the interface ( $\phi = 0.5$ ) is indicated by a red solid line. (b) Wave elevation profiles of the two-dimensional solitary wave. Symbols represent simulation results using `isoPhi` (circles), `gradPhi` (crosses), and `plicRDF` (diamonds), while solid lines show the theoretical solution from potential flow theory. Colors correspond to probe locations at  $x = 30$  (black), 40 (cyan), 50 (yellow), 60 (purple), and 70 m (pink).

TABLE I: Configuration of the (a) base grid and (b) refinement zones. In (a),  $y$  indicates the vertical extent of each subdomain, and  $N_y$  denotes the number of grid cells in the vertical direction. The total expansion ratio  $\Gamma$  represents the ratio between the largest and smallest cell heights. In (b),  $\theta$  indicates the refinement level in each Cartesian direction, where  $\theta = \log_2(\Delta_{\text{base}}/\Delta_{\text{refined}})$ .

(a)

	Top			Middle			Bottom		
	$y$ (m)	$N_y$	$\Gamma$	$y$ (m)	$N_y$	$\Gamma$	$y$ (m)	$N_y$	$\Gamma$
$G1$	[0.54, 0.84]	50	10	[0.5, 0.54]	25	1	[0.0, 0.5]	30	40
$G2$	[0.54, 0.84]	60	18	[0.5, 0.54]	50	1	[0.0, 0.5]	40	50
$G3$	[0.54, 0.84]	60	35	[0.5, 0.54]	100	1	[0.0, 0.5]	40	80

(b)

	$y$ (m)	$(\theta_x, \theta_y, \theta_z)$
$R1$	[0.49, 0.58]	(2, 0, 1)
$R2$	[0.5, 0.55]	(3, 0, 2)

### 1. Simulation setup

First, the simulation setup for the reference-scale case is described. The computational domain has dimensions  $L_x = 7.0$  m in the streamwise direction,  $L_y = 0.84$  m in the vertical direction, and  $L_z = 0.08$  m in the spanwise direction. The grid resolution is  $N_x = 700$  points in the streamwise direction and  $N_z = 10$  points in the spanwise direction. In the vertical direction, the domain is divided

into three subdomains: top, middle, and bottom. The top and bottom regions are predominantly occupied by air and water, respectively, while the middle region contains the air–water interface. The middle subdomain is discretized uniformly, whereas the top and bottom subdomains employ stretched grids with increasing cell sizes away from the interface. Details of the grid configuration for each subdomain are provided in Table I(a).

As an example, in the  $G3$  configuration, the middle region uses a uniform grid spacing of  $\Delta y = 4.0 \times 10^{-4}$  m. In the top subdomain, the grid is stretched with a total expansion ratio  $\Gamma = \Delta y_{\text{max}}/\Delta y_{\text{min}} = 35$ , yielding  $\Delta y_{\text{max}} = 1.8 \times 10^{-2}$  m near the top boundary and  $\Delta y_{\text{min}} = 5.15 \times 10^{-4}$  m at the interface with the middle region. The corresponding local cell-to-cell expansion ratio is approximately 1.0621. This base grid is further refined using local refinement windows, as summarized in Table I(b). Refinement levels in each direction are denoted by  $(\theta_x, \theta_y, \theta_z)$ , where  $\theta = \log_2(\Delta_{\text{base}}/\Delta_{\text{refined}})$ . In total, four combinations of base grid and refinement level are considered:  $(G1, R1)$ ,  $(G2, R1)$ ,  $(G3, R1)$ , and  $(G3, R2)$ .

The target wave parameters are a wavelength  $\lambda = 0.81$  m, wave height  $H = 0.04$  m, and mean water depth  $h = 0.52$  m, corresponding to one of the experimental conditions reported by Buckley and Veron [46]. The left boundary at  $x = 0.0$  m serves as the inlet and is divided vertically, with  $y \leq 0.54$  m designated as the wave inlet and  $y > 0.54$  m as the wind inlet. Similarly, at the right boundary ( $x = 7.0$  m),  $y \leq 0.54$  m defines the wave outlet and  $y > 0.54$  m defines the wind outlet.

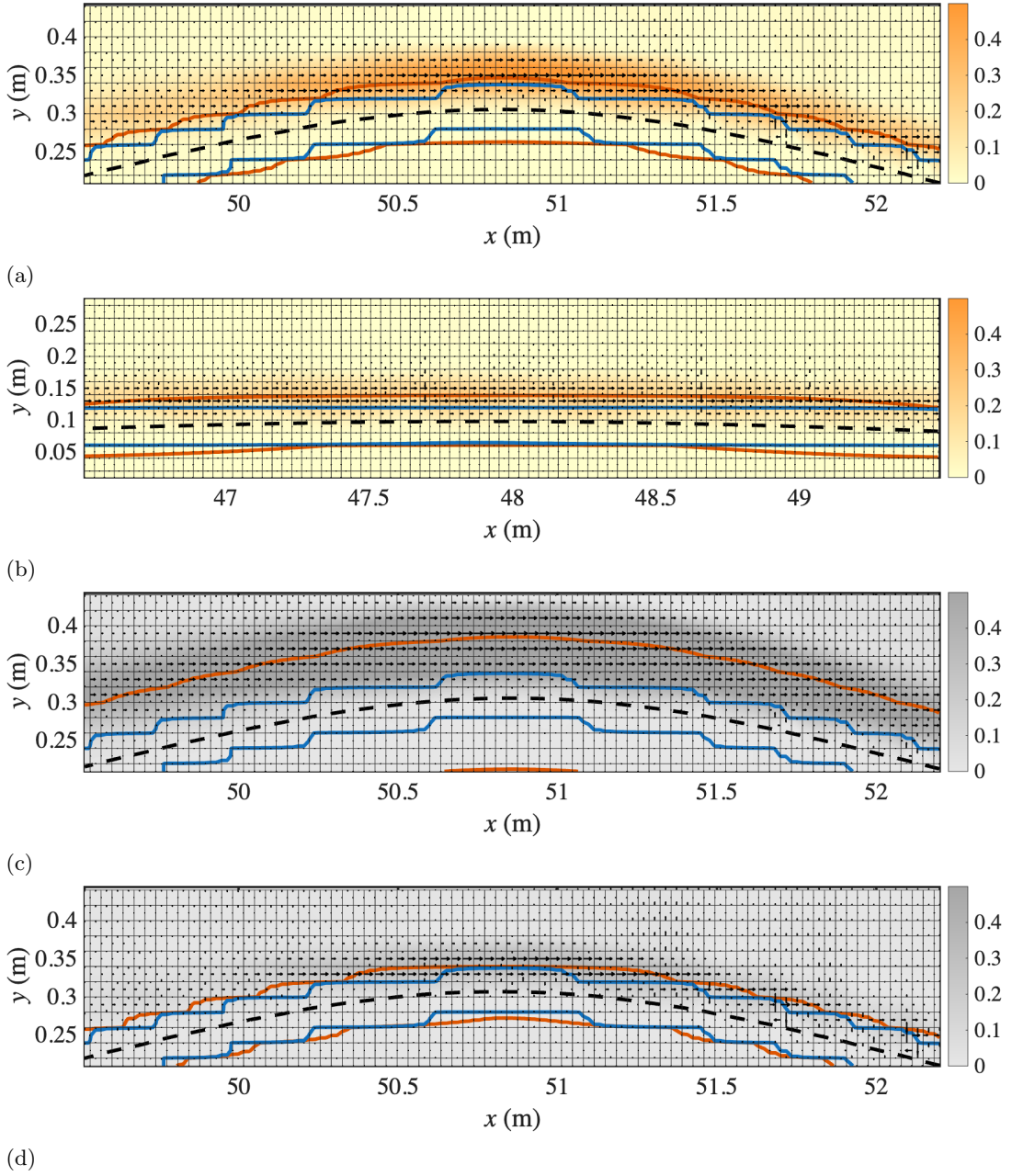


FIG. 12: Comparison of face flux differences between `isoPhi` and `gradPhi`, calculated as  $F_{\text{MULES}} - F_{\text{ISO}}$ , near the crest of the solitary wave. Panels show (a)  $A/H = 0.3$  with  $C_\alpha = 1.0$ , (b)  $A/H = 0.1$  with  $C_\alpha = 1.0$ , (c)  $A/H = 0.3$  with reduced compression velocity  $C_\alpha = 0.1$ , and (d)  $A/H = 0.3$  with increased compression velocity  $C_\alpha = 2.0$ . Flux difference magnitude is shown as a colormap, while face flux vectors are indicated by black arrows at cell faces. Cell face outlines are shown in black. Iso-contours of the phase indicator are displayed for  $\phi = 0.5$  (black-dashed), and  $\phi = 0.1, 0.9$  for `isoPhi` (blue) and `gradPhi` (red).

The wave field is prescribed at the wave inlet using first-order Stokes wave theory as a Dirichlet boundary condition, propagating toward the outlet, where an absorbing boundary condition is applied to minimize wave reflections. For the wind field, a constant streamwise velocity of  $u = 0.05 \text{ m, s}^{-1}$  is imposed at the wind inlet. To mitigate artificial vortex generation near the interface,

a linear vertical interpolation of velocity is applied between the wave crest and the bottom of the wind inlet. A Neumann-type boundary condition is avoided at the wind inlet, as it produces an uncontrolled inflow velocity profile that is highly sensitive to the interface-capturing method. A slip condition is applied at the top boundary, periodic conditions are imposed in the spanwise direc-

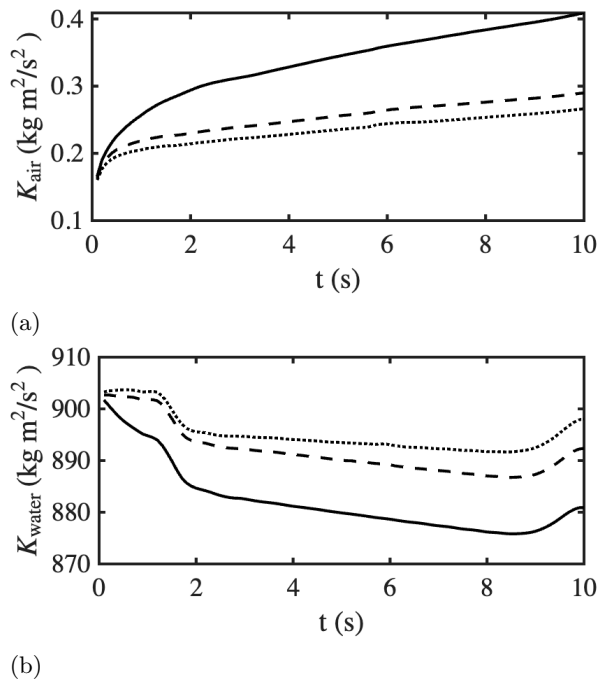


FIG. 13: Total kinetic energy in the (a) air phase and (b) water phase during solitary wave simulations. Black lines correspond to different values of the compression velocity coefficient:  $C_\alpha = 0.1$  (solid),  $C_\alpha = 1.0$  (dashed), and  $C_\alpha = 2.0$  (dotted).

tion, and a Neumann-type condition is enforced at the wind outlet.

For the larger-scale configuration, a tenfold geometric scaling is applied to simulate a larger wave case. The scaled wave parameters are a wave period  $T = 2.616$  s, wavelength  $\lambda = 8.1$  m, wave height  $H = 0.4$  m, and mean water depth  $h = 5.2$  m. Consequently, the wave celerity increases from 1.1 m/s to 3.51 m/s. All domain dimensions and boundary conditions are scaled proportionally.

### 2. High wave-age waves at small scale

We first examine the instantaneous wave profile to investigate the manifestation of spurious currents. Fig. 14 shows the instantaneous velocity fields at  $t = 20$  s for all interface-capturing methods using the  $(G3, R1)$  grid. For the *isoPhi* approach, which has been shown to generate the highest spurious current magnitude among the three methods, we observe clear velocity disturbances near the interface within the lighter fluid (air) region. In contrast, both *plicRDF* and *gradPhi* exhibit significantly smoother instantaneous velocity fields, indicating the absence of grid-scale numerical noise that is prominently observed in *isoPhi*. However, we emphasize that the smoothness of the velocity field does not inherently guarantee physical accuracy.

To further highlight this effect, we present additional

results for *isoPhi* on a finer  $(G3, R2)$  grid. Qualitatively, the finer resolution reveals higher-frequency velocity oscillations and slightly amplified spurious currents, consistent with the curvature error scaling observed in Section III A 3. As demonstrated in Sections III B and IV A, the impact of spurious current becomes more significant when its magnitude is comparable to the characteristic velocity of the system. While large-scale waves with low curvature and negligible surface tension force compared to the inertia force may not be heavily affected, in laboratory-scale or low-Reynolds-number simulations, this influence can be considerable.

The analysis proceeds with phase-averaged stress fields for the wave-coherent and turbulent components, shown in Fig. 15. The wave-coherent stress at this resolution and wave celerity, differences between *plicRDF* and *gradPhi* in stress fields are negligible. However, the *isoPhi* method exhibits diminished positive stress on both the windward and leeward sides of the wave, consistent with the presence of spurious currents that persist regardless of grid refinement (cf. Section III A 3). For the turbulent stress fields shown in the second column of Fig. 15, all methods exhibit weak turbulence generation, consistent with the relatively low wave celerity. The *isoPhi* method fails to capture the positive stress on the leeward side near the troughs and shows only weak asymmetry in the positive stress region beyond the crests. The *gradPhi* method predicts stronger positive stress than *plicRDF*, although both exhibit similar spatial distributions.

### 3. Grid convergence of vertical profiles

To demonstrate the conclusions from the previous sections, vertical profiles of the phase-independent mean velocity ( $\bar{U}$ ), wave-coherent stress ( $\bar{R}$ ), and turbulent stress ( $R'$ ) for each interface-capturing method are presented across four grid configurations:  $(G1, R1)$ ,  $(G2, R1)$ ,  $(G3, R1)$ , and  $(G3, R2)$ , as shown in Fig. 16. The finest grid configuration does not include additional refinement in the vertical direction. The mean velocity and stress components are normalized by the wave celerity and its square, respectively. Snapshots for phase-averaging were collected within the region  $x = 3.8$  m to 5.8 m.

For the phase-independent mean velocity, *isoPhi* displays notable kinks, reflecting the influence of spurious currents. These profiles do not exhibit convergence under grid refinement. In contrast, *gradPhi* shows a clear convergence trend, with a local maximum above the interface becoming more pronounced on finer grids. This behavior is also observed in *plicRDF*, which exhibits smoother convergence toward a similar profile, albeit with a slightly lower maximum velocity. The larger maximum velocity predicted by *gradPhi* compared to *plicRDF* is attributed to the additional flux induced by interface regularization. As the grid is refined, *gradPhi* exhibits relatively rapid asymptotic convergence, consistent with the findings re-

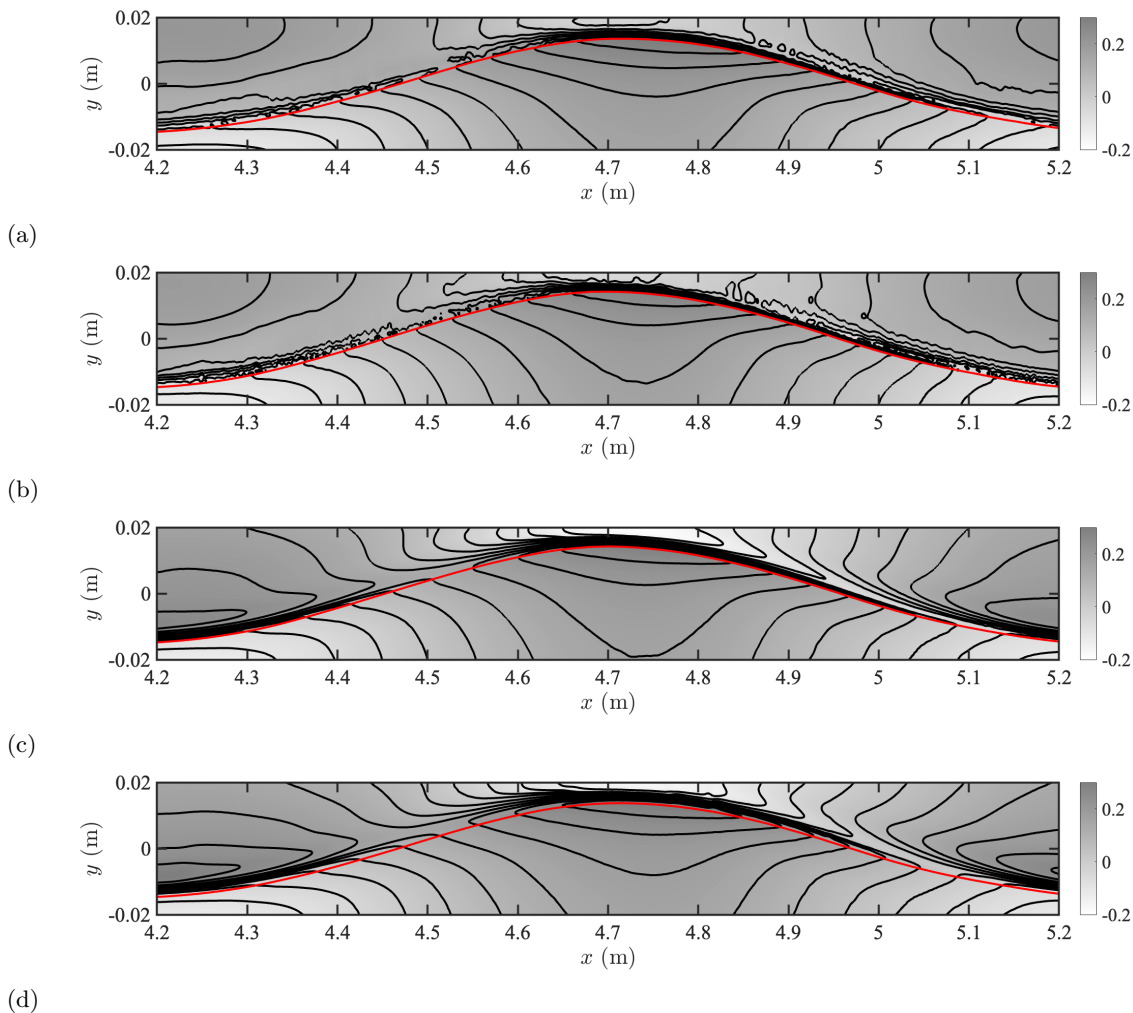


FIG. 14: Instantaneous velocity field of monochromatic wave simulations at  $t = 20$  s in the region  $x \in [4.2, 5.2]$  m. Panels show (a) `isoPhi` with the  $(G3, R1)$  grid, (b) `isoPhi` with the  $(G3, R2)$  grid, (c) `plicRDF`, and (d) `gradPhi`. The colormap represents velocity magnitude, and the interface ( $\phi = 0.5$ ) is denoted by the red solid line.

ported in the previous sections.

For the wave-coherent stress, all methods exhibit similar vertical trends, with local maxima located slightly above the interface that shift closer to it as the resolution increases. The `isoPhi` method underpredicts the stress magnitude, whereas `plicRDF` yields the highest values, nearly twice those of `isoPhi`. Given the negligible wind speed at the inlet, these stress differences correlate with variations in wave height in the phase-averaged fields. The measured wave heights are  $3.78 \times 10^{-2}$  m (`isoPhi`),  $3.85 \times 10^{-2}$  m (`plicRDF`), and  $3.75 \times 10^{-2}$  m (`gradPhi`). The slightly larger wave height predicted by `plicRDF` (approximately 2% greater than that predicted by `gradPhi`) contributes to the corresponding enhancement of the wave-coherent stress. In contrast, the similar wave heights obtained with `isoPhi` and `gradPhi` indicate that the stress underprediction in `isoPhi` originates from contamination by spurious currents.

The turbulent stresses for all three methods exhibit

asymptotic convergence, although the converged profiles differ among approaches. Their magnitude is on the order of  $O(10^{-4})$  and remains negligible under the present wind-wave conditions. These differences become more pronounced in high wave-age cases with turbulent wind inlet conditions, which are examined in the section below.

#### 4. Comparison with large-scale simulations

Larger-scale waves correspond to a relatively coarser mesh resolution for the wind fields, as well as higher wave celerity compared to the reference case. This configuration therefore provides a suitable framework to examine how the error sources identified in Section III manifest in the monochromatic wave setup. The phase-averaged streamwise velocity fields are shown in Fig. 17 for the reference scale and in Fig. 18 for the larger scale. Both simulations employ the  $(G3, R1)$  grid configuration, with the

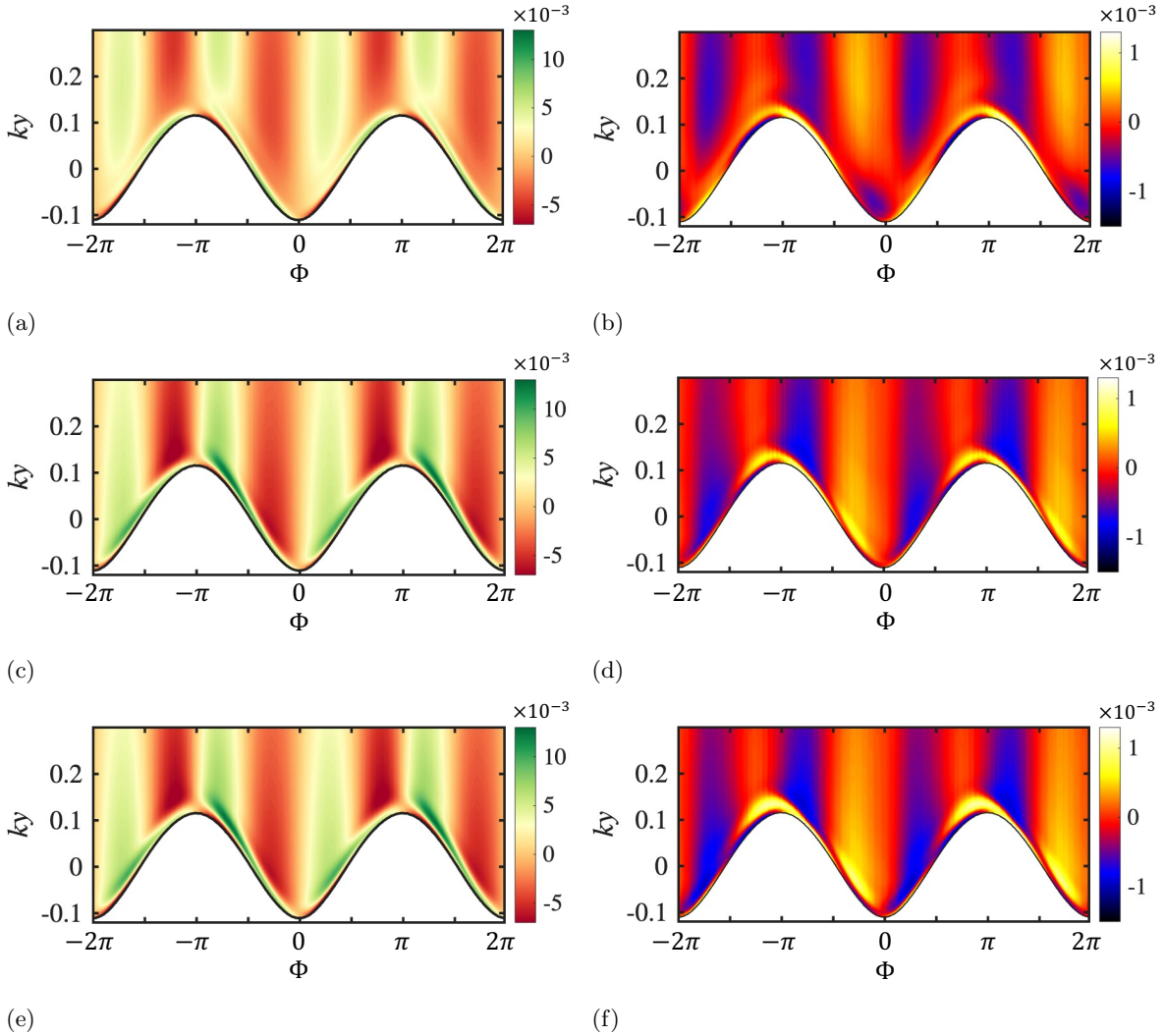


FIG. 15: Wave-coherent (first column) and turbulent (second column) Reynolds stress fields for each interface-capturing method. Results are presented for (a–b) `isoPhi`, (c–d) `plicRDF`, and (e–f) `gradPhi`. The interface ( $\phi = 0.5$ ) is indicated by black solid lines.

large-wave case having grid spacings that are ten times larger in physical scale.

In Fig. 17(a–b), the `isoPhi` results show significant deviations from the velocity fields of `plicRDF` and `gradPhi` in Fig. 17(c–d), respectively. Across all interface-capturing methods, the airflow in proximity to the interface tends to follow the wave-induced motion, characterized by positive streamwise velocity above wave crests and negative velocity above troughs. Further away from the interface, this trend reverses, exhibiting negative velocity above crests and positive velocity above troughs. Among the methods, `isoPhi` demonstrates noticeably smoother transitions toward the maximum level of positive and negative velocity region, suggesting that spurious currents can significantly distort the phase-averaged mean flow when their magnitude becomes comparable to wave-induced velocities.

Phase-averaged streamwise velocity fields for larger

scale configuration are shown in Fig. 18. In the `isoPhi` results, the off-interface velocity anomalies observed in the smaller-scale case shift closer to the interface. In contrast, the `gradPhi` solution exhibits thickened velocity layers near both the crest and trough, with smoother gradients and a broadened region of positive streamwise velocity between successive wave crests. This behavior is consistent with enhanced momentum transport induced by interface regularization. For `plicRDF`, thickening of the positive velocity layer is observed near the trough region while maintaining relatively sharp gradients. Compared to the reference scale, where the difference between `plicRDF` and `gradPhi` is marginal, a noticeable discrepancy emerges at the larger scale, reflecting the sensitivity of the compression term to the coarser grid resolution. These findings imply that spurious currents diminish in impact with increased wave scale and interface transport velocity; however, artificial flux layers aligned with inter-

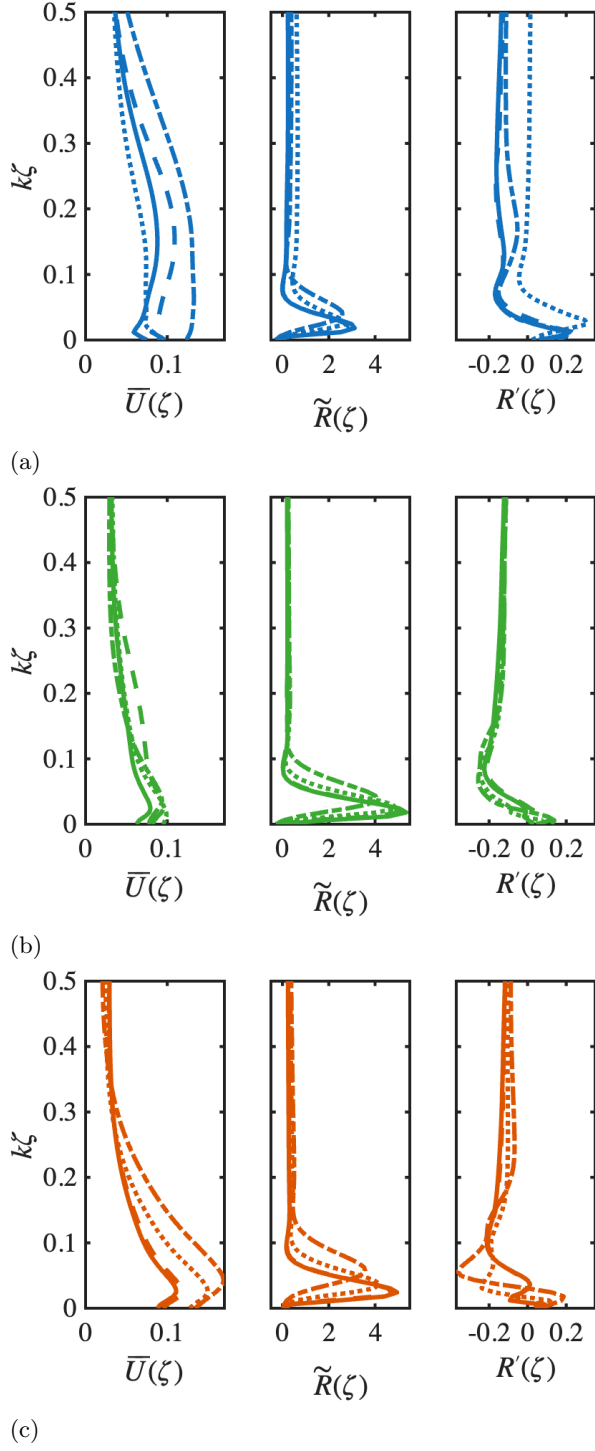


FIG. 16: Vertical profiles of the phase-independent mean velocity, wave-coherent stress, and turbulent stress for each column, respectively. Subfigures show results from (a) `isoPhi`, (b) `plicRDF`, and (c) `gradPhi`. Line types indicate grid configurations, ( $G1, R1$ ) (dash-dotted), ( $G2, R1$ ) (dotted), ( $G3, R1$ ) (dash), and ( $G3, R2$ ) (solid).

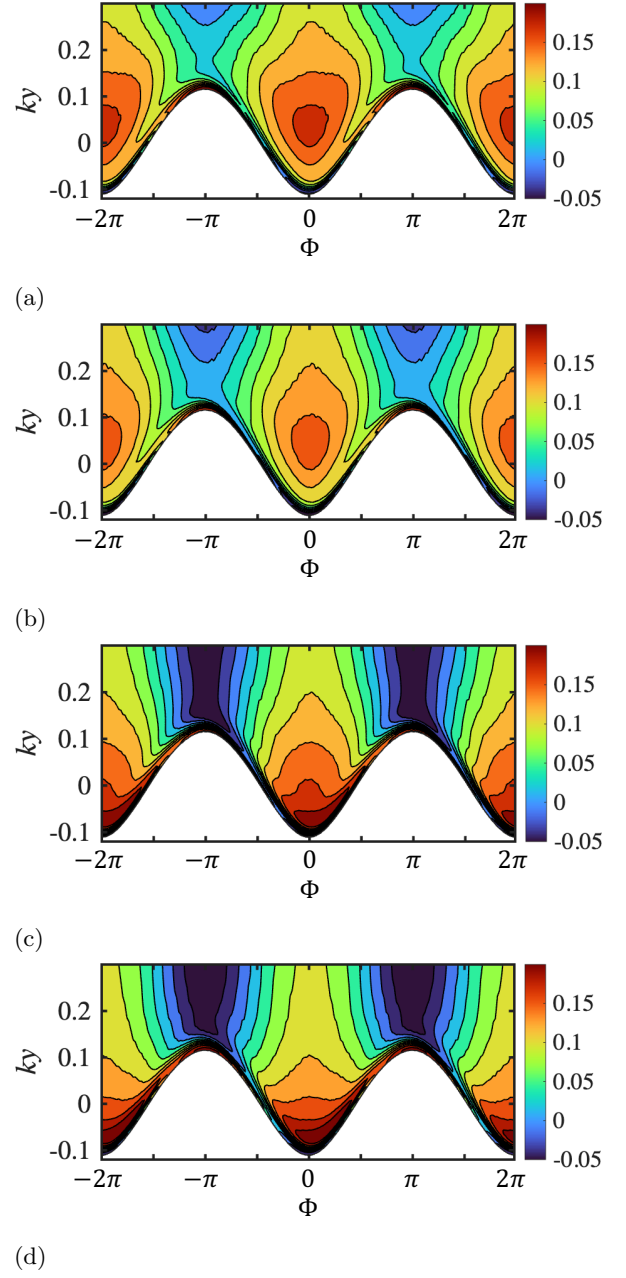


FIG. 17: Phase-averaged streamwise velocity field for simulations with different interface-capturing methods. Shown are (a) `isoPhi` with the ( $G3, R1$ ) grid, (b) `isoPhi` with the ( $G3, R2$ ) grid, (c) `plicRDF`, and (d) `gradPhi`. The colormap indicates the magnitude of the phase-averaged velocity.

face motion may still arise due to discretization effects.

In conclusion, spurious currents manifest strongly in phase-independent and wave-coherent vertical profiles and can substantially affect velocity prediction in lighter fluids. In coarser grids, artificial compression methods such as `gradPhi` produce excessive phase-independent velocities aligned with interface motion. While signs of convergence are observed for each component, additional

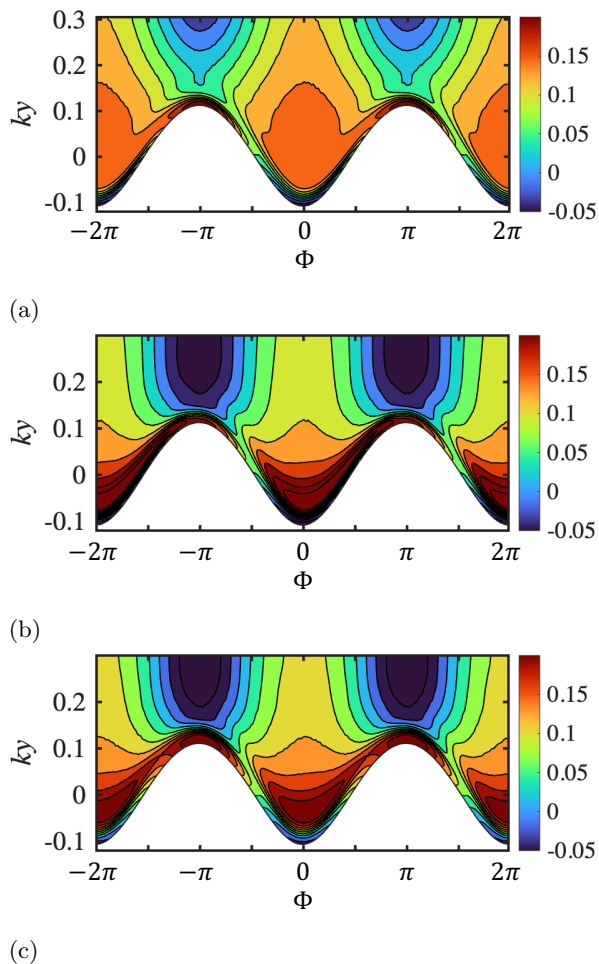


FIG. 18: Phase-averaged streamwise velocity fields for geometrically scaled-up monochromatic wave simulations. Results are shown for (a) `isoPhi`, (b) `plicRDF`, and (c) `gradPhi`, all using the  $(G3, R1)$  grid with a tenfold geometric wave scaling. The colormap represents velocity magnitude.

refinement would be necessary to confirm asymptotic behavior.

### C. Validation against experimental data

We validate our simulation results against experimental data from Buckley and Veron [46] under combined wind-wave conditions.

#### 1. Simulation setup

The simulation setup, including the wave configuration, follows that described in Section IV B, except for the wind inlet condition. For the wind inlet, we employ the divergence-free synthetic eddy method (DFSEM) proposed by Poletto *et al.* [47], which introduces realis-

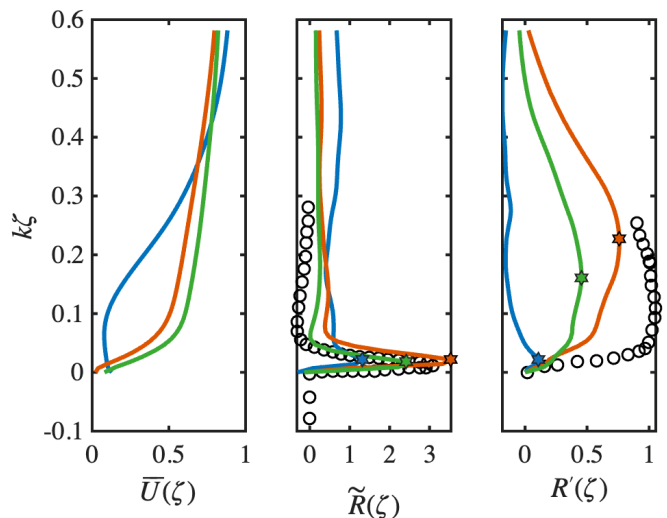


FIG. 19: Vertical profiles from the old wave simulation, decomposed into (left) phase-independent mean velocity, (middle) wave-coherent stress, and (right) turbulent stress. Lines represent results from `isoPhi` (blue), `plicRDF` (green), and `gradPhi` (red). Black circles indicate experimental reference data from Buckley and Veron [46]. Maximum values of the stress components are indicated by symbols.

tic turbulence by superimposing synthetic eddies on a mean velocity profile. The mean profile follows the standard logarithmic law for wall-bounded flows, expressed as  $u(y) = (u^*/\kappa) \log((y + y_0)/y_0)$ , where  $u^* = 0.041$  m/s is the friction velocity,  $\kappa = 0.41$  is the von Kármán constant, and  $y_0 = 1.5 \times 10^{-5}$  m is the roughness length of the interface. The Reynolds stress components used for turbulence generation at the inlet are  $(R_{xx}, R_{xy}, R_{xz}, R_{yy}, R_{yz}, R_{zz}) = (0.01, -0.001681, 0.0, 0.0025, 0.0, 0.0064)$  m<sup>2</sup>/s<sup>2</sup>. The velocity and stresses are normalized by  $u^*$  and its square, respectively.

#### 2. Comparison of stress fields

The comparison of the interface-capturing methods for the vertical profiles is shown in Fig. 19. First, no reference data exist for the phase-independent component of the mean velocity. Therefore, it is only compared among the different approaches. Notably, the `isoPhi` results show a different profile near the interface ( $k\zeta < 0.1$ ), exhibiting an inflection point, whereas the other two approaches display similar profiles.

Next, the experimental data indicate that the wave-coherent stress reaches a maximum value approximately three times the total stress ( $\tilde{R} \approx 3.1$ ). Although the predicted peak location ( $k\zeta \approx 0.018$ ) is slightly higher than the reference value ( $k\zeta \approx 0.011$ ), all approaches yield maximum values sufficiently close to the reference location, within less than the smallest grid spac-

ing. However, their magnitudes differ: `isoPhi` predicts  $\bar{R} \approx 1.31$ , `plicRDF` predicts  $\bar{R} \approx 2.42$ , and `gradPhi` predicts  $\bar{R} \approx 3.54$ . The slightly larger maximum value predicted by `gradPhi` may be attributed to artificial flux near the wave crest, as discussed in Section IV B. We also note that none of the approaches accurately capture the slightly negative stress values beyond the maximum point, farther away from the surface [8].

For the turbulent stress, all approaches consistently underestimate the magnitude at all vertical locations. The `isoPhi` approach predicts negative stress immediately away from the interface. Although the `plicRDF` and `gradPhi` approaches predict a region of positive stress, both fail to capture the strong gradient near the interface, and their peak magnitudes and locations deviate significantly from the reference data.

To investigate the origin of this deviation, we compare the spatial distribution of stresses between the simulation and the experimental data. Only the results obtained using the `plicRDF` method are presented and shown in Fig. 20. The comparison of the wave-coherent stress field illustrates that `plicRDF` successfully identifies the narrow region of positive stress near the interface [20]. The maximum positive stress on the windward side is slightly weaker in the simulations, which contributes to the slightly smaller peak observed in the vertical profiles. Nonetheless, the overall stress distribution and its approximate magnitude are satisfactorily captured.

For the turbulent stress components, the simulation qualitatively captures a negative–positive pattern near the interface. However, two critical features evident in the stress distribution in Fig. 20 are missing, leading to a severe underprediction of the vertical profile in Fig. 19. First, the magnitude of the positive stress near the interface on the leeward side is weak. Second, the stress away from the interface appears nearly symmetric rather than asymmetric. Similar behavior is observed in the `gradPhi` results (not shown). This discrepancy may arise from several factors, such as the grid aspect ratio or the accuracy of the wind inlet profile. Recall that this fast-moving wave is expected to generate a positive stress region on the leeward side because the relative wind speed is slower than the wave speed. However, this stress may dissipate too quickly beyond the crest. Another possible source of this error is insufficient resolution near the interface, as the smallest grid spacing,  $\Delta y_{\min} \approx 10.9l_\nu$ , is much larger than the viscous length scale  $l_\nu = 3.66 \times 10^{-5}$  m. These issues are beyond the scope of the present study.

In conclusion, comparison with the experimental data of Buckley and Veron [46] yields several important findings. First, the results reaffirm that spurious currents must be effectively mitigated when the wind and wave velocities are of comparable magnitude, as they significantly distort both the mean and fluctuating components of the flow. In addition, the interface regularization term contributes to the slight overprediction of wave-coherent stress by enhancing the mass flux above the crest under non-negligible wind conditions. Second, the overall spa-

tial structures of both the wave-coherent and turbulent stress fields are reproduced with reasonable agreement to the experimental measurements, indicating that the dominant flow features are captured. Third, although the current grid resolution resolves the thin stress layers associated with the wave-coherent stress, it fails to reproduce the asymmetry of the turbulent stress. In particular, the stress level on the leeward side remains insufficient to sustain turbulence, and it decays rapidly beyond the crest. The implications of this underprediction require further examination, since resolving the detailed mechanisms of turbulent generation at the interface would substantially increase the computational cost and may limit the practical feasibility of such simulations.

## V. CONCLUSIONS

In this study, we conducted a comprehensive investigation into the effects of spurious current and interface regularization on wind–wave simulations under high wave-age conditions. Our findings highlight how two critical numerical factors substantially influence wind–wave simulations. The first factor concerns the generation of spurious currents arising from curvature-calculation errors. All examined methods exhibit a lack of curvature-error convergence under grid refinement, resulting in persistent spurious velocities in the vicinity of the interface. When the magnitude of these unphysical currents approaches that of the mean flow, they contaminate all components of the triple decomposition, most notably the phase-independent mean velocity. We show that improving curvature estimation by replacing the `isoPhi` method with the `plicRDF` method significantly enhances simulation accuracy, reduces wave dissipation, and restores asymptotic convergence with grid refinement. This issue is particularly relevant to laboratory-scale validation studies, where waves are characterized by relatively low wave celerity and high curvature. Under such conditions, curvature effects become non-negligible. Curvature-induced errors may appear secondary in inertia-dominated wave regimes, where interface transport remains largely unaffected. However, the present results show that they become critical when wind-induced turbulence is considered at comparable length scales. Although the turbulent component remains underpredicted even at the finest resolution, the overall agreement with the experimental data improves substantially when the RDF-based approach is employed.

The second critical factor is the artificial mass flux introduced by the interface regularization. The `gradPhi` approach, which is representative of interface-sharpening schemes more broadly, generates an additional flux layer in under-resolved simulations. The thickness of this artificial flux layer is comparable to the numerical interface thickness, and its magnitude scales with the local interface-transport velocity. As a result, even in high-speed flows, this artificial flux becomes non-negligible

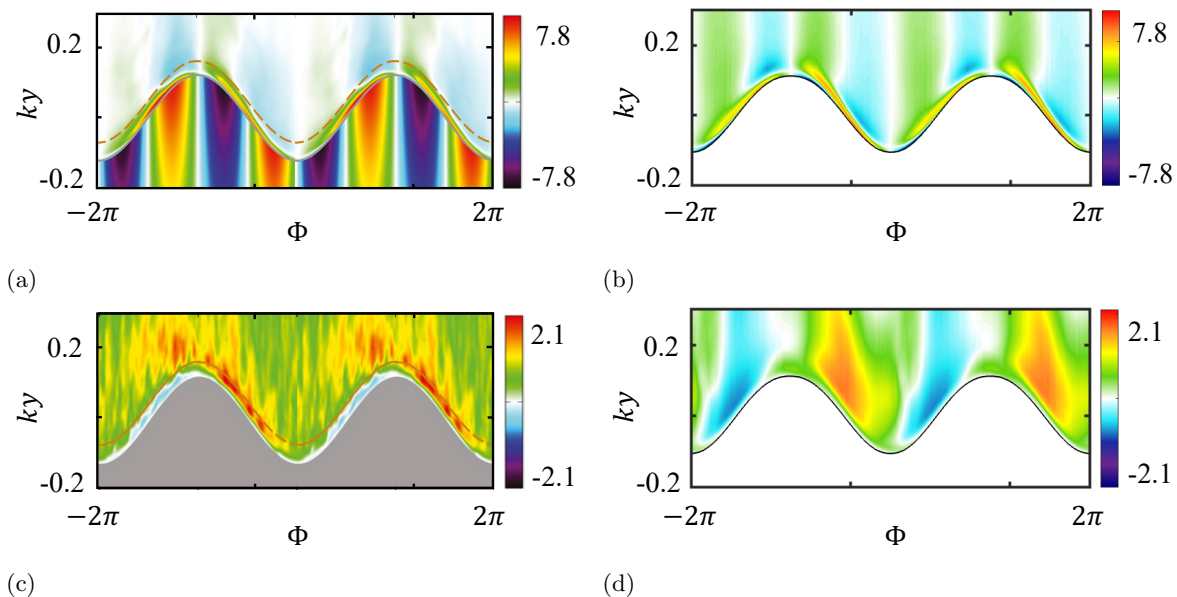


FIG. 20: (a,b) Normalized phase-averaged wave-coherent stress and (c,d) turbulent stress from the old wave simulation. Colormaps depict the stress distributions. Simulation results (b,d) are compared with the experimental reference data from Buckley and Veron [46]. Gray and orange dashed lines indicate the inner and critical layers, respectively. © American Meteorological Society. Used with permission.

when the grid resolution is insufficient. The effects of these factors accumulate across both time and space because of the continuous interaction between the wind and the surface waves throughout the computational domain. Clear signatures of the resulting errors appear in phase-averaged fields and in their corresponding vertical profiles.

## ACKNOWLEDGMENTS

This study was supported by the National Science Foundation under Grant No. CMMI-21311961. The authors acknowledge the Stanford Research Computing Center for providing computational resources and technical support that contributed to these results.

## Appendix A: Interface reconstruction

To utilize the isoAdvect algorithm introduced in Section II B 1, the interface normal vector  $n_{\mathcal{F}(p),i}$  and interface velocity  $u_{\mathcal{F}(p),i}$  must be obtained through interface reconstruction. Details of the reconstruction methods are described in Scheufler and Roenby [33]. For completeness, we summarize two reconstruction procedures here. One is based directly on the phase indicator field and the other utilizes the RDF.

### 1. $\phi$ -Based reconstruction

The procedure for identifying the  $\phi_p$ -isoface is outlined as follows:

1. Identify interface cells that satisfy  $\epsilon < \phi_p < 1 - \epsilon$ , where  $\epsilon$  is a specified tolerance used to define interface cells. In this study, we set  $\epsilon = 10^{-8}$ .
2. Interpolate the phase indicator  $\phi$  to the vertices of the cell. The volume fraction of phase 1 at vertex  $f_v$  is calculated as

$$f_v = \frac{\sum_{k \in C_v} w_k \phi_k}{\sum_{k \in C_v} w_k}, \quad (\text{A1})$$

where  $w_k$  denotes the inverse distance weights,  $k$  is a vertex index, and  $C_v$  represents the set of vertices connected to vertex  $v$ .

3. Iterate on all cell edges to determine the intersection points corresponding to a target volume fraction value  $\phi_p^*$ . The value of  $\phi_p^*$  may be selected from one of the interpolated vertex values  $f_v$ .
4. For each cell face, the identified intersection points are connected across faces to form an intersection line, e.g.,  $\overline{I'I'}$  in Fig. 1.
5. These intersection lines are then connected to construct the periphery of the polygonal face, for example, the blue plane shown in Fig. 1. Note that it is not guaranteed to form a planar face.

6. Compute the submerged volume  $V(\phi_p^*)$  of the interface cell. Steps 3 to 5 are repeated iteratively, updating  $\phi_p^*$  at each iteration, until the condition  $V(\phi_p^*)/V_{cv} = \phi_p$  is satisfied. It is important to note that  $\phi_p$  and  $\phi_p^*$  are not necessarily equal.
7. Calculate the centroid  $x_{\mathcal{F}(p),i}$  and the unit normal vector  $n_{\mathcal{F}(p),i}$  of the  $\phi_p$ -isoface. The isoface is a planar  $N_v$ -gonal surface composed of  $N_v$  vertices, which together form  $N_v$  sub-triangles sharing a common average point. The face normal vector is computed as the sum of the normals of the sub-triangles

$$n_{\mathcal{F}(p),i} = \sum_{k=1}^{N_v} n_{k,i} = \sum_{k=1}^{N_v} \frac{1}{2} (x_{k+1,i} - x_{k,i}) \times (\bar{x}_i - x_{k,i}), \quad (\text{A2})$$

and the centroid of the isoface is computed as the area-weighted average of the sub-triangle centers

$$x_{\mathcal{F}(p),i} = \sum_{k=1}^{N_v} \frac{|n_{k,i}|}{|n_{\mathcal{F}(p),i}|} \left( \frac{x_{k+1,i} + x_{k,i} + \bar{x}_i}{3} \right), \quad (\text{A3})$$

where  $\bar{x}_i = \frac{1}{N_v} \sum_{k=1}^{N_v} x_{k,i}$  is the geometric center of all vertices, and  $n_{k,i}$  is the normal vector of each sub-triangle.

The unit normal vector of the  $\phi_p$ -isoface is then given by

$$\hat{n}_{\mathcal{F}(p),i} = \frac{n_{\mathcal{F}(p),i}}{|n_{\mathcal{F}(p),i}|}. \quad (\text{A4})$$

8. Decompose the cell into tetrahedra, each sharing the cell center as a common vertex. Once the tetrahedron containing the isoface center  $x_{\mathcal{F}(p),i}$  is identified, the interface velocity  $u_{\mathcal{F}(p),i}$  is obtained by linear interpolation from the velocity values at the vertices of that tetrahedron.

As mentioned earlier, although geometric VOF-type methods provide a sharp representation of the interface, they often yield inaccurate curvature estimates due to their reliance on the large gradient of the phase indicator across the interface.

## 2. RDF-based reconstruction

To mitigate the inaccurate curvature calculation issue, a signed-distance-like function has been proposed to reconstruct a smoother auxiliary variable, enabling more accurate curvature estimation and reducing spurious velocity artifacts [44]. In this context, Scheufler and Roenby [33] proposed a residual-based iterative approach to compute the face center  $x_{\mathcal{F}(p),i}$  and unit normal vector  $n_{\mathcal{F}(p),i}$  more accurately.

The procedure is as follows:

1. Initialize the interface normal  $n_{\mathcal{F}(p),i}$  using either the value from the previous time step or the gradient of the phase indicator field.
2. If the interface is sufficiently resolved (e.g., see Eq. (18) in Scheufler and Roenby [33]), determine the face center  $x_{\mathcal{F}(p),i}$  by following the steps outlined in Section A 1, with the following two modifications:

First, replace the interpolation in Eq. (A1) with the projected distances to each vertex of cell  $p$ ,

$$d_k = x_{k,i} n_{\mathcal{F}(p),i}, \quad (\text{A5})$$

where  $x_{k,i}$  is the position of vertex  $k$  and  $n_{\mathcal{F}(p),i}$  is the current estimate of the interface normal.

Second, instead of computing the normal from Eq. (A2), directly use the defined interface normal  $n_{\mathcal{F}(p),i}$  for reconstruction.

3. Construct the RDF,  $\Psi_p$ , at the center of cell  $p$  as

$$\Psi_p = \frac{\sum_q w_{pq} \tilde{\Psi}_{pq}}{\sum_q w_{pq}}, \quad (\text{A6})$$

where the summation is taken over neighboring interface cells  $q$ . The interface distance contribution from each neighboring cell  $q$  is defined as,

$$\tilde{\Psi}_{pq} = n_{\mathcal{F}(q),i} (x_{p,i} - x_{\mathcal{F}(q),i}), \quad (\text{A7})$$

where  $x_{p,i}$  denotes the centroid of cell  $p$ , and  $x_{\mathcal{F}(q),i}$  and  $n_{\mathcal{F}(q),i}$  are the centroid and unit normal of the  $\phi$ -isoface in neighboring cell  $q$ , respectively.

The weights  $w_{pq}$  are calculated based on the alignment between the interface direction and the distance vector:

$$w_{pq} = \frac{|n_{\mathcal{F}(q),i} (x_{p,i} - x_{\mathcal{F}(q),i})|^2}{|x_{p,i} - x_{\mathcal{F}(q),i}|^2}. \quad (\text{A8})$$

4. Update the interface normal using the gradient of the RDF,

$$n_{\mathcal{F}(p),i} = \frac{\partial \Psi / \partial x_i}{|\partial \Psi / \partial x_i|}. \quad (\text{A9})$$

5. Repeat steps 2 to 4 iteratively until the normal interface change between successive iterations falls below the prescribed tolerance.

Due to the smooth nature of the RDF field, this method provides more reliable and accurate interface normals, particularly in regions where the interface curvature plays a critical role in flow dynamics.

## Appendix B: Wave-following coordinate

The coordinates  $(\xi, \zeta)$  define a wave-following reference frame, which adapts to the shape of the surface waves, as illustrated in Fig. 2. Various formulations exist for constructing such coordinates, including those proposed by Shen and Yue [48] and Buckley and Veron [46]. Following the latter, we define the wave-following coordinate system as

$$\xi(x, z) = x - i \sum_n a_n \exp[i(k_n \xi + \phi_n)] \exp(-k_n \zeta), \quad (\text{B1})$$

$$\zeta(x, z) = z - \sum_n a_n \exp[i(k_n \xi + \phi_n)] \exp(-k_n \zeta), \quad (\text{B2})$$

where  $a_n$ ,  $k_n$ , and  $\phi_n$  represent the amplitude, wavenumber, and phase of the  $n$ -th Fourier mode, respectively.

These coefficients are obtained from the Fourier decomposition of the wave elevation  $\eta(\mathbf{x}, t)$ , expressed as

$$\eta(\xi) = \sum_n a_n \exp[i(k_n \xi + \phi_n)]. \quad (\text{B3})$$

The velocity field  $\mathbf{u}$  is then interpolated from the original Cartesian coordinate system to the wave-following coordinate system.

For discretized surface points located at  $x = x_0$ , the corresponding wave-following coordinate is  $\xi = \xi_{x_0}$ , since  $x_0 = \xi_{x_0}$  at  $\zeta = 0$  (cf. Eq.(B2)). The phase domain  $\Phi \in [0, 2\pi]$  is uniformly divided into  $N_{\text{bins}}$  intervals. Using Eq.(19), the instantaneous phase of the wave at each interpolated velocity point  $\mathbf{u}(\xi_{x_0}, \zeta)$  is evaluated, and the corresponding velocity data are sorted into the appropriate phase bins. The phase-averaged velocity field  $\langle \mathbf{u} \rangle(\xi, \zeta)$  is then obtained by averaging within each bin.

- 
- [1] W. Huang, H. Xiao, G. Bryan, and R. Rotunno, Numerical modeling of dynamic wave force acting on Ecambia bay bridge deck during hurricane Ivan, *Journal of Waterway, Port, Coastal, and Ocean Engineering* **135**, 164 (2009).
  - [2] N. Chini, P. Stansby, J. Leake, J. Wolf, J. Roberts-Jones, and J. Lowe, The impact of sea level rise and climate change on inshore wave climate: A case study for east anglia (uk), *Coastal Engineering* **57**, 973 (2010).
  - [3] G. Dodet, A. Melet, F. Ardhuin, X. Bertin, D. Idier, and R. Almar, The contribution of wind-generated waves to coastal sea-level changes, *Surveys in Geophysics* **40**, 1563 (2019).
  - [4] Ø. Breivik, K. Mogensen, J.-R. Bidlot, M. A. Balmaseda, and P. A. Janssen, Surface wave effects in the nemo ocean model: Forced and coupled experiments, *Journal of Geophysical Research: Oceans* **120**, 2973 (2015).
  - [5] J. G. Powers, J. B. Klemp, W. C. Skamarock, C. A. Davis, J. Dudhia, D. O. Gill, J. L. Coen, D. J. Gochis, R. Ahmadov, S. E. Peckham, *et al.*, The weather research and forecasting model: Overview, system efforts, and future directions, *Bulletin of the American Meteorological Society* **98**, 1717 (2017).
  - [6] T. Hara and S. E. Belcher, Wind forcing in the equilibrium range of wind-wave spectra, *Journal of Fluid Mechanics* **470**, 223 (2002).
  - [7] J. B. Edson, V. Jampana, R. A. Weller, S. P. Bigorre, A. J. Plueddemann, C. W. Fairall, S. D. Miller, L. Mahrt, D. Vickers, and H. Hersbach, On the exchange of momentum over the open ocean, *Journal of Physical Oceanography* **43**, 1589 (2013).
  - [8] P. P. Sullivan, J. C. McWilliams, and C.-H. Moeng, Simulation of turbulent flow over idealized water waves, *Journal of Fluid Mechanics* **404**, 47 (2000).
  - [9] D. Yang and L. Shen, Direct-simulation-based study of turbulent flow over various wavy boundaries, *Journal of Fluid Mechanics* **650**, 131 (2010).
  - [10] P. P. Sullivan, J. C. McWilliams, and E. G. Patton, Large-eddy simulation of marine atmospheric boundary layers above a spectrum of moving waves, *Journal of the Atmospheric Sciences* **71**, 4001 (2014).
  - [11] T. Hara and P. P. Sullivan, Wave boundary layer turbulence over surface waves in a strongly forced condition, *Journal of Physical Oceanography* **45**, 868 (2015).
  - [12] T. Cao and L. Shen, A numerical and theoretical study of wind over fast-propagating water waves, *Journal of Fluid Mechanics* **919**, A38 (2021).
  - [13] M.-Y. Lin, C.-H. Moeng, W.-T. Tsai, P. P. Sullivan, and S. E. Belcher, Direct numerical simulation of wind-wave generation processes, *Journal of Fluid Mechanics* **616**, 1 (2008).
  - [14] N. Suzuki, T. Hara, and P. P. Sullivan, Impact of breaking wave form drag on near-surface turbulence and drag coefficient over young seas at high winds, *Journal of physical oceanography* **43**, 324 (2013).
  - [15] P. P. Sullivan, M. L. Banner, R. P. Morison, and W. L. Peirson, Turbulent flow over steep steady and unsteady waves under strong wind forcing, *Journal of Physical Oceanography* **48**, 3 (2018).
  - [16] E. L. Andreas, Sea spray and the turbulent air-sea heat fluxes, *Journal of Geophysical Research: Oceans* **97**, 11429 (1992).
  - [17] L. H. Holthuijsen, M. D. Powell, and J. D. Pietrzak, Wind and waves in extreme hurricanes, *Journal of Geophysical Research: Oceans* **117** (2012).
  - [18] V. K. Makin, A note on the drag of the sea surface at hurricane winds, *Boundary-layer meteorology* **115**, 169 (2005).
  - [19] M. L. Banner and W. K. Melville, On the separation of air flow over water waves, *J. Comput. Phys.* **77**, 825 (1976).
  - [20] S. Belcher and J. Hunt, Turbulent flow over hills and waves, *Annual Review of Fluid Mechanics* **30**, 507 (1998).
  - [21] M. L. Banner and W. L. Peirson, Tangential stress beneath wind-driven air-water interfaces, *J. Comput. Phys.* **364**, 115 (1998).
  - [22] Z. Yang, B.-Q. Deng, and L. Shen, Direct numerical simulation of wind turbulence over breaking waves, *J. Comput. Phys.* **850**, 120 (2018).
  - [23] C. Song and A. I. Sirviente, A numerical study of break-

- ing waves, *Physics of fluids* **16**, 2649 (2004).
- [24] A. Iafrazi, A. Babanin, and M. Onorato, Modulational instability, wave breaking, and formation of large-scale dipoles in the atmosphere, *Physical review letters* **110**, 184504 (2013).
- [25] N. Ren, Y. Li, and J. Ou, Coupled wind-wave time domain analysis of floating offshore wind turbine based on computational fluid dynamics method, *Journal of Renewable and Sustainable Energy* **6** (2014).
- [26] Y. Liu, Q. Xiao, A. Incecik, C. Peyrard, and D. Wan, Establishing a fully coupled CFD analysis tool for floating offshore wind turbines, *Renewable Energy* **112** (2017).
- [27] H. Park, T. Do, T. Tomiczek, D. T. Cox, and J. W. van de Lindt, Numerical modeling of non-breaking, impulsive breaking, and broken wave interaction with elevated coastal structures: laboratory validation and inter-model comparisons, *Ocean Engineering* **158**, 78 (2018).
- [28] S. Osher and J. A. Sethian, Fronts propagating with curvature-dependent speed: Algorithms based on hamilton-jacobi formulations, *Journal of computational physics* **79**, 12 (1988).
- [29] C. W. Hirt and B. D. Nichols, Volume of fluid (vof) method for the dynamics of free boundaries, *Journal of computational physics* **39**, 201 (1981).
- [30] C. Liu and J. Shen, A phase field model for the mixture of two incompressible fluids and its approximation by a fourier-spectral method, *Physica D: Nonlinear Phenomena* **179**, 211 (2003).
- [31] H. Hwang and S. S. Jain, A robust phase-field method for two-phase flows on unstructured grids, *arXiv preprint arXiv:2310.10795* (2023).
- [32] J. Roenby, H. Bredmose, and H. Jasak, A computational method for sharp interface advection, *Royal Society open science* **3**, 160405 (2016).
- [33] H. Scheufler and J. Roenby, Accurate and efficient surface reconstruction from volume fraction data on general meshes, *Journal of computational physics* **383**, 1 (2019).
- [34] P. Higuera, Application of computational fluid dynamics to wave action on structures, PhD. Universidade de Cantabria (2015).
- [35] J. U. Brackbill, D. B. Kothe, and C. Zemach, A continuum method for modeling surface tension, *J. Comput. Phys.* **100**, 335 (1991).
- [36] M. M. Francois, S. J. Cummins, E. D. Dendy, D. B. Kothe, J. M. Sicilian, and M. W. Williams, A balanced-force algorithm for continuous and sharp interfacial surface tension models within a volume tracking framework, *Journal of Computational Physics* **213**, 141 (2006).
- [37] P. Higuera, J. L. Lara, and I. J. Losada, Realistic wave generation and active wave absorption for navier–stokes models: Application to openfoam®, *Coast. Eng.* **71**, 102 (2013).
- [38] S. Márquez Damián, N. M. Nigro, P. Bohorquez Rodríguez de Medina, M. I. Cantero, J. D’Elia, A. Larretguy, and M. A. Storti, *An extended mixture model for the simultaneous treatment of short and long scale interfaces*, Ph.D. thesis, Universidad Nacional del Litoral (2013).
- [39] L. Jofre, R. Borrell, O. Lehmkuhl, and A. Oliva, Parallel load balancing strategy for Volume-of-Fluid methods on 3-D unstructured meshes, *Journal of Computational Physics* **282**, 269 (2015).
- [40] S. T. Zalesak, Fully multidimensional flux-corrected transport algorithms for fluids, *Journal of computational physics* **31**, 335 (1979).
- [41] W. A. Gardner and E. A. Robinson, *Statistical spectral analysis—A nonprobabilistic theory* (1989).
- [42] T. Abadie, J. Aubin, and D. Legendre, On the combined effects of surface tension force calculation and interface advection on spurious currents within volume of fluid and level set frameworks, *Journal of Computational Physics* **297**, 611 (2015).
- [43] L. Gamet, M. Scala, J. Roenby, H. Scheufler, and J.-L. Pierson, Validation of volume-of-fluid openfoam® isoadvector solvers using single bubble benchmarks, *Computers & Fluids* **213**, 104722 (2020).
- [44] S. J. Cummins, M. M. Francois, and D. B. Kothe, Estimating curvature from volume fractions, *Computers & structures* **83**, 425 (2005).
- [45] E. V. Laitone, The second approximation to cnoidal and solitary waves, *Journal of fluid mechanics* **9**, 430 (1960).
- [46] M. P. Buckley and F. Veron, Structure of the airflow above surface waves, *J. Phys. Oceanogr.* **46**, 1377 (2016).
- [47] R. Poletto, T. Craft, and A. Revell, A new divergence free synthetic eddy method for the reproduction of inlet flow conditions for les, *Flow, turbulence and combustion* **91**, 519 (2013).
- [48] L. Shen and D. K. P. Yue, Large-eddy simulation of free-surface turbulence, *J. Fluid Mech.* **440**, 75 (2001).